Research Square

Preprints are preliminary reports that have not undergone peer review.
They should not be considered conclusive, used to inform clinical practice,
or referenced by the media as validated information.

Silicon Phase Shifter Modeling for Electronic-Photonic Co-Simulation in a 250 nm EPIC BiCMOS Technology

Tobias Schwabe

schwabet@hni.uni-paderborn.de

University of Paderborn

Daniel Steckler

Leibniz Institute for High Performance Microelectronics

Christian Kress

University of Paderborn

Stephan Kruse

University of Paderborn

Lars Zimmermann

Leibniz Institute for High Performance Microelectronics

J. Christoph Scheytt

University of Paderborn

Research Article

Keywords: silicon photonics phase shifter, data communication, modeling, electro-optic transmitter, optical modulator, electro-optic simulation

Posted Date: July 15th, 2026

DOI: https://doi.org/10.21203/rs.3.rs-9690075/v1

License: This work is licensed under a Creative Commons Attribution 4.0 International License.
Read Full License

Additional Declarations: No competing interests reported.

Silicon Phase Shifter Modeling for Electronic-Photonic Co-Simulation in a 250 nm EPIC BiCMOS Technology

Tobias Schwabe [0000-0001-5478-5446] [1,2*], Daniel Steckler [0000-0001-9645-1807] [3], Christian Kress [0000-0002-4403-2237] [1,2], Stephan Kruse [0000-0001-6525-4683] [1,2], Lars Zimmermann[3], J. Christoph Scheytt [0000-0002-5950-6618] [1,2]

[1*]Heinz Nixdorf Institute, Department of Electrical Engineering, Paderborn University, Fürstenallee 11, Paderborn, 33102, NRW, Germany.
[2]Institute for Photonic Quantum Systems, Paderborn University, Warburger Str. 100, Paderborn, 33102, NRW, Germany.
[3]Leibniz Institute for High Performance Microelectronics, Im Technologiepark 25, Frankfurt (Oder), 15236, Brandenburg, Germany.

*Corresponding author(s). E-mail(s): schwabet@hni.uni-paderborn.de;
Contributing authors: steckler@ihp-microelectronics.com;
christian.kress@uni-paderborn.de; stkruse@hni.uni-paderborn.de;
lzimmermann@ihp-microelectronics.com; cscheytt@hni.uni-paderborn.de;

Abstract

A physical model of an electro-optic silicon phase shifter (PS) in an electronic-photonic integrated circuit (EPIC) technology platform is derived and implemented using a hardware description language (HDL). The model enables SPICE-compatible electro-optic co-simulations using common integrated circuit (IC) design software. The physically oriented modeling approach enables the linking of PS geometries and doping concentrations to PS parameters and characteristics. In a novel approach, extending the consideration of pn-junctions in silicon PSs from abrupt to non-uniform profiles revealed a physical interpretation of a SPICE diode model parameter previously treated phenomenologically and established correlations with the electro-optical properties of the PSs. Analytical results, simulations, and measurements are compared and consolidated into a compact and scalable PS model. Through HDL implementation, the model facilitates accurate and efficient co-design and co-simulation of electro-optic systems using modern IC design software. A systematic parameter-fitting scheme is presented and applied to two different PSs with distinct doping profiles in a commercially available EPIC bipolar complementary metal-oxide-semiconductor (BiCMOS) technology. Additionally, the accuracy of the model is demonstrated by simulating a complete electro-optic transmitter with data rates of up to 80 Gb/s, showing excellent agreement between simulation and measurement.

Keywords: silicon photonics phase shifter, data communication, modeling, electro-optic transmitter, optical modulator, electro-optic simulation

1 Introduction

Phase shifters (PSs) using the free-carrier plasma dispersion (FCPD) effect are fundamental components in silicon photonics, enabling precise high-speed control of light propagation in integrated photonic circuits. Therefore, they enable modulation of optical data signals by means of Mach-Zehnder modulators (MZMs) and ring modulators, which are key components in electro-optic transmitters. While photonic electromagnetic (EM) simulation tools allow for modeling and parameter extraction of strongly idealized PSs with homogeneous materials and boundaries [1–3], they generally do not align well with manufactured devices and are therefore not applicable to accurate chip design and system development. In this work, the developed model is based on measurements of manufactured devices and is implemented in SPICE-compatible [4] hardware description language (HDL) to allow efficient electro-optic co-simulation and integrated circuit (IC) design with conventional electronic design automation (EDA) software. Unlike conventional EDA-compatible, phenomenological models, the developed PS model captures physical effects within the PS and links parameters to geometric dimensions and material properties. It reveals links between common diode SPICE model parameters, which are well-established in modeling, to electro-optic properties. Moreover, a parameter fitting process is presented and applied to two PSs in a commercially available 250 nm electronic-photonic integrated circuit (EPIC) BiCMOS technology [5]. Therefore, the derived results can be directly transferred into the technology's process design kit. A novel approach, which takes into account not only abrupt but also non-uniform pn-junctions, describes charge distribution and space-charge-region (SCR) expansion, considers continuity of all important physical quantities in multiple operation regions, and allows capturing of deviations from ideal operation due to tolerances and parasitics. It enables simulation and modeling in a wide operation range. Furthermore, the robust model helps understanding trade-offs and is applied to investigate bottlenecks. This is demonstrated by a PS doping profile improvement, which is consistent with the physical model and leads to a higher bandwidth in simulations and in measurements. The PS model is applied to a high-speed broadband electro-optic transmitter with data rates up to 80 Gb/s and it is shown that transient and S-parameter simulations of the transmitter are in-line with transmitter measurements, when using the proposed PS model.

In Section 2, the PS model is introduced and an equivalent circuit is derived. All incorporated physical effects are investigated and explained. A detailed description of all mathematical correlations and model parameters is given and further discussed in Section 3, which is also presenting an improved PS doping profile. It is followed by Section 4, which presents the measurement setup that was used to analyze two different PSs. The measurement results are used in Section 5, which discusses the parameter fitting process in which the model is fitted to the measurement results. Afterwards, in Section 6, a proof of the PS model is presented. The PS model is applied to a high-speed broadband electro-optic transmitter and it is shown that transient and S-parameter simulations of the transmitter are in-line with transmitter measurements, when using the developed PS model. Finally, Section 7 concludes and summarizes all results.

2 Phase shifter model

As depicted in Fig. 1, the PS consists of a rib waveguide with p and n dopings. Thus, a pn-junction diode is formed inside an optical waveguide.

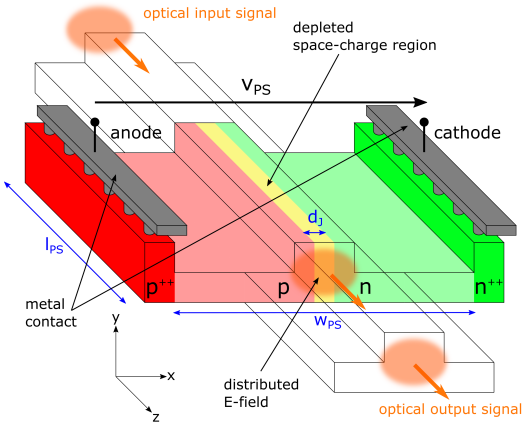


Fig. 1 FCPD based silicon PS geometry including input and output waveguides

In the following, a corresponding PS equivalent circuit, which is presented in Fig. 2, is derived.

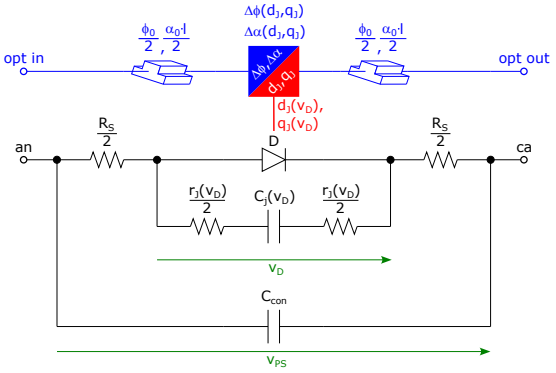


Fig. 2 Reverse-biased PS equivalent circuit

2.1 Electrical modeling

Since the PS includes a pn-junction, the electrical equivalent circuit is similar to conventional diode equivalent circuits. A series resistance R_S models the contact resistance and the ohmic behavior of the semiconductor material, whereas an ideal diode D, which follows the Shockley equation (given in (1)), models the ideal, lossless diode operation [6–8].

$$i_D = I_S \cdot \left(e^{\frac{v_D}{n_D \cdot V_T}} - 1 \right) \tag{1}$$

where i_D denotes the diode current, v_D the diode voltage, I_S the saturation current, n_D the ideality factor, and $V_T = k_B T/e$ the thermal voltage.
As shown in Fig. 2, the parasitic capacitance between the anode and cathode contact metalizations is modeled by a constant capacitance C_{con}.
Assuming an ideal diode without any crystal defects or impurities, an abrupt pn-junction in x-direction with homogeneous p-doping for $x < 0$, homogeneous n-doping for $x > 0$, and neglecting any charge carriers in the SCR, because their charge is negligibly small compared to the ionized dopant atoms, the space charge density can be approximated by [6–8]:

$$\rho^{ideal} \approx \begin{cases} -e \cdot N_A^- & -x_p^{ideal} \le x < 0 \\ e \cdot N_D^+ & 0 < x \le x_n^{ideal} \end{cases} \tag{2}$$

where e denotes the elementary charge, N_D^+ the ionized donor density, N_A^- the ionized acceptor density, x_p the SCR expansion into the p-doped region, and x_n the SCR expansion into the n-doped region (see Fig. 3a).
Accurate modeling of the space charge density is essential for describing the charge distribution and junction capacitance correctly. Therefore, a more general approach is chosen to improve modeling accuracy and to capture variations in the space charge density ρ, which can result from non-homogeneous dopant distributions and defects:

$$\rho = \begin{cases} -e \cdot C_A \cdot |x|^M, & -x_p \le x < 0 \\ e \cdot C_D \cdot |x|^M, & 0 < x \le x_n \end{cases} \tag{3}$$

with C_A, C_D and M being defect and doping concentration dependent parameters.
Therefore, the abrupt pn-junction in (2) follows as a special case of (3) with $M = 0$, $C_D = N_D^+$, and $C_A = N_A^-$ and is presented by the blue graph in Fig. 3b.
Applying Poisson's equation

$$\frac{d^2\varphi}{dx^2} = -\frac{\rho}{\epsilon} \tag{4}$$

to (3) and considering

$$\frac{d\varphi}{dx} = -E \tag{5}$$

results in:

$$\begin{aligned} E(x) &= \begin{cases} -\int_{-x_p}^{x} \frac{eC_A}{\epsilon} \cdot |\tilde{x}|^M \, d\tilde{x}, & -x_p \le x < 0 \\ \int_{x_n}^{x} \frac{eC_D}{\epsilon} \cdot |\tilde{x}|^M \, d\tilde{x}, & 0 < x \le x_n \end{cases} \\ &= \begin{cases} -\frac{eC_A}{\epsilon(M+1)} \cdot (x_p^{M+1} - |x|^{M+1}), & -x_p \le x < 0 \\ -\frac{eC_D}{\epsilon(M+1)} \cdot (x_n^{M+1} - x^{M+1}), & 0 < x \le x_n \end{cases} \end{aligned} \tag{6}$$

where ϵ denotes the permittivity, φ the electric potential, and E the electric field.
Considering continuity of E at $x = 0$ in (6) yields

$$C_A \cdot x_p^{M+1} = C_D \cdot x_n^{M+1}. \tag{7}$$

With (5) and (6), the electric potential φ is given by:

$$\varphi(x) = -\int_0^x E(\tilde{x})\,\mathrm{d}\tilde{x}$$
$$= \begin{cases} \frac{eC_\mathrm{A}}{\epsilon(M+1)}\left(x_\mathrm{p}^{M+1}x + \frac{(-x)^{M+2}}{M+2}\right), & -x_\mathrm{p} \le x < 0 \\ \frac{eC_\mathrm{D}}{\epsilon(M+1)}\left(x_\mathrm{n}^{M+1}x - \frac{x^{M+2}}{M+2}\right), & 0 < x \le x_\mathrm{n} \end{cases} \tag{8}$$

The results of (3), (6), and (8) for different gradient coefficients M are presented in Fig. 3b, 3c, and 3d.

The voltage across the pn-junction $\varphi_\mathrm{J} - v_\mathrm{D}$ is obtained as:

$$\varphi_\mathrm{J} - v_\mathrm{D} = \varphi(x_\mathrm{n}) - \varphi(-x_\mathrm{p})$$
$$= \frac{e}{\epsilon} \cdot \frac{1}{M+2} \cdot \left(C_\mathrm{D} \cdot x_\mathrm{n}^{M+2} + C_\mathrm{A} \cdot x_\mathrm{p}^{M+2}\right) \tag{9}$$

where φ_J denotes the built-in junction potential and v_D the externally applied voltage.
As depicted in Fig. 3a, the total SCR width d_J is

$$d_\mathrm{J} = x_\mathrm{n} + x_\mathrm{p}. \tag{10}$$

With (7) and (10) it follows:

$$d_\mathrm{J} = x_\mathrm{p} \cdot \left(1 + \sqrt[M+1]{\frac{C_\mathrm{A}}{C_\mathrm{D}}}\right) = x_\mathrm{n} \cdot \left(1 + \sqrt[M+1]{\frac{C_\mathrm{D}}{C_\mathrm{A}}}\right) \tag{11}$$

Applying (11) to (9) leads to:

$$\varphi_\mathrm{J} - v_\mathrm{D} = \frac{d_\mathrm{J}^{M+2} e}{\epsilon(M+2)\left(\frac{1}{\sqrt[M+1]{C_\mathrm{D}}} + \frac{1}{\sqrt[M+1]{C_\mathrm{A}}}\right)^{M+1}} \tag{12}$$

Therefrom, the SCR width d_J results as:

$$d_\mathrm{J} = d_\mathrm{J0} \cdot \sqrt[M+2]{1 - \frac{v_\mathrm{D}}{\varphi_\mathrm{J}}} \tag{13}$$

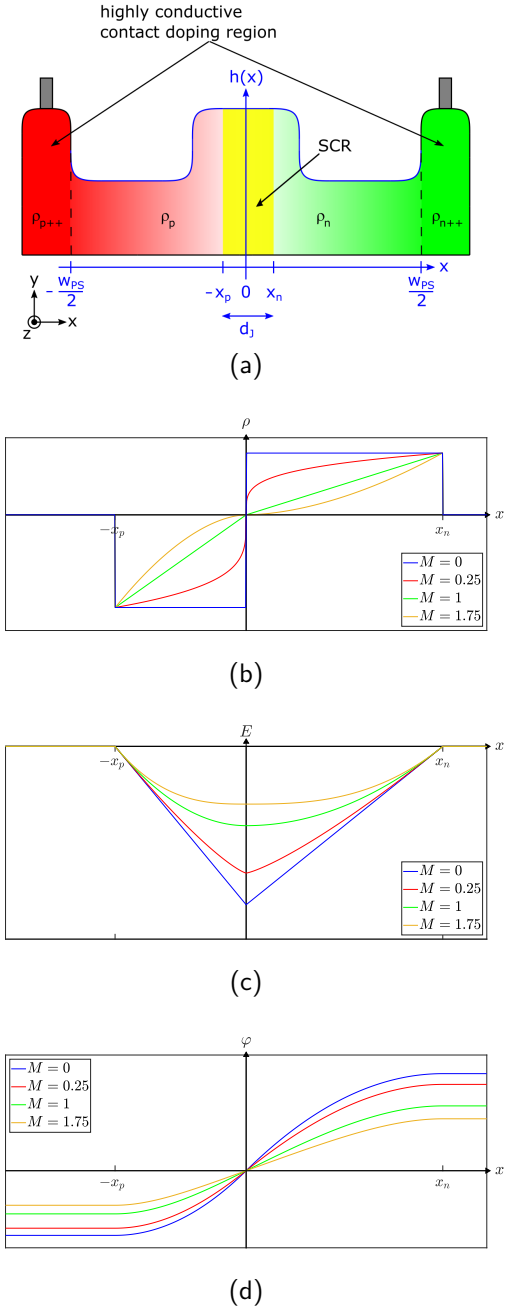


Fig. 3 (a) Illustration of doping concentrations and geometric parameters, (b) Space charge density, (c) Electric field, and (d) Potential in the PS for different gradient factors M, normalized to same SCR width

with the zero-voltage SCR width

$$d_\mathrm{J0} = \sqrt[M+2]{(M+2) \cdot \frac{\epsilon \cdot \varphi_\mathrm{J}}{e}}$$
$$\cdot \sqrt[M+2]{\left(\frac{1}{\sqrt[M+1]{C_\mathrm{D}}} + \frac{1}{\sqrt[M+1]{C_\mathrm{A}}}\right)^{M+1}} \tag{14}$$

In case of an abrupt pn-junction with $M = 0$, $C_\mathrm{D} = N_\mathrm{D}^+$, and $C_\mathrm{A} = N_\mathrm{A}^-$ according to (2), the SCR width simplifies to

$$d_{\mathrm{J}0} = \sqrt[2]{2 \cdot \frac{\epsilon \cdot \varphi_\mathrm{J}}{e} \cdot \left(\frac{1}{N_\mathrm{D}^+} + \frac{1}{N_\mathrm{A}^-} \right)} \tag{15}$$

which is in line with findings in [6], [8], and [9].
A linearly graded pn-junction with $M = 1$ and $C = C_\mathrm{A} = C_\mathrm{D}$ leads to

$$d_{\mathrm{J}0} = \sqrt[3]{12 \cdot \frac{\epsilon \cdot \varphi_\mathrm{J}}{e} \cdot \frac{1}{C}} \tag{16}$$

which is in line with findings in [9].
The junction charge q_J represents the deviation in the number of free charges when the applied voltage equals the junction potential ($v_\mathrm{D} = \varphi_\mathrm{J}$) and the effectively SCR vanishes. Since the number of free charges in the pn-junction decreases as the SCR width increases, the junction charge q_J is negative by definition and is described by:

$$q_\mathrm{J} = -A_\mathrm{J} \cdot \int_{x_\mathrm{p}}^{0} \rho \, \mathrm{d}x = -A_\mathrm{J} \cdot \int_{0}^{x_\mathrm{n}} \rho \, \mathrm{d}x \tag{17}$$

with $A_\mathrm{J} = h_\mathrm{PS} \cdot l_\mathrm{PS}$ being the area spanned by the PS height h_PS and length l_PS.
Applying (3) yields:

$$q_\mathrm{J} = -\frac{eA_\mathrm{J}C_\mathrm{A}x_\mathrm{p}^{M+1}}{M+1} = -\frac{eA_\mathrm{J}C_\mathrm{D}x_\mathrm{n}^{M+1}}{M+1} \tag{18}$$

With (11) and (13), x_n and x_p can be expressed as:

$$x_\mathrm{n} = \frac{d_\mathrm{J}}{1 + \sqrt[M+1]{\frac{C_\mathrm{D}}{C_\mathrm{A}}}} = \frac{d_{\mathrm{J}0}}{1 + \sqrt[M+1]{\frac{C_\mathrm{D}}{C_\mathrm{A}}}} \cdot \sqrt[M+2]{1 - \frac{v_\mathrm{D}}{\varphi_\mathrm{J}}} \tag{19}$$

$$x_\mathrm{p} = \frac{d_\mathrm{J}}{1 + \sqrt[M+1]{\frac{C_\mathrm{A}}{C_\mathrm{D}}}} = \frac{d_{\mathrm{J}0}}{1 + \sqrt[M+1]{\frac{C_\mathrm{A}}{C_\mathrm{D}}}} \cdot \sqrt[M+2]{1 - \frac{v_\mathrm{D}}{\varphi_\mathrm{J}}} \tag{20}$$

Inserting (19) into (18) yields

$$q_\mathrm{J} = -A_\mathrm{J} \cdot \frac{e}{M+1} \cdot \frac{d_\mathrm{J}^{M+1}}{\left(\frac{1}{\sqrt[M+1]{C_\mathrm{D}}} + \frac{1}{\sqrt[M+1]{C_\mathrm{A}}} \right)^{M+1}} \tag{21}$$

which can be expressed as

$$q_\mathrm{J} = q_{\mathrm{J}0} \cdot \left(1 - \frac{v_\mathrm{D}}{\varphi_\mathrm{J}} \right)^{\frac{M+1}{M+2}} \tag{22}$$

with the zero-voltage junction charge

$$q_{\mathrm{J}0} = -A_\mathrm{J} \cdot \frac{e}{M+1} \frac{d_{\mathrm{J}0}^{M+1}}{\left(\frac{1}{\sqrt[M+1]{C_\mathrm{D}}} + \frac{1}{\sqrt[M+1]{C_\mathrm{A}}} \right)^{M+1}} \tag{23}$$

Since the junction capacitance C_j is defined as the derivative of the junction charge q_J with respect to the applied voltage v_D, it results as:

$$\begin{aligned} C_j &= \frac{\mathrm{d}q_\mathrm{J}}{\mathrm{d}v_\mathrm{D}} = -\frac{q_{\mathrm{J}0}}{\varphi_\mathrm{J}} \cdot \frac{M+1}{M+2} \cdot \frac{1}{\sqrt[M+2]{1 - \frac{v_\mathrm{D}}{\varphi_\mathrm{J}}}} \\ &= C_{j0} \cdot \frac{1}{\sqrt[M+2]{1 - \frac{v_\mathrm{D}}{\varphi_\mathrm{J}}}} \end{aligned} \tag{24}$$

with the zero-voltage junction capacitance

$$\begin{aligned} C_{\mathrm{j}0} &= -\frac{q_{\mathrm{J}0}}{\varphi_\mathrm{J}} \cdot \frac{M+1}{M+2} \\ &= A_\mathrm{J} \cdot \frac{e}{\varphi_\mathrm{J}} \cdot \frac{1}{M+2} \frac{d_{\mathrm{J}0}^{M+1}}{\left(\frac{1}{\sqrt[M+1]{C_\mathrm{D}}} + \frac{1}{\sqrt[M+1]{C_\mathrm{A}}} \right)^{M+1}} \end{aligned} \tag{25}$$

Inserting (14) yields:

$$\begin{aligned} C_{\mathrm{j}0} &= \sqrt[M+2]{\frac{eA_\mathrm{J}^{M+2}\epsilon^{M+1}}{\varphi_\mathrm{J}(M+2)\left(\frac{1}{\sqrt[M+1]{C_\mathrm{D}}} + \frac{1}{\sqrt[M+1]{C_\mathrm{A}}} \right)^{M+1}}} \\ &= A_\mathrm{J} \cdot \frac{\epsilon}{d_{\mathrm{J}0}} \end{aligned} \tag{26}$$

A common way of modeling a junction capacitance C_j in SPICE is to use a gradient coefficient M_C and describe it as follows [6]:

$$C_\mathrm{j} = C_{\mathrm{j}0} \cdot \frac{1}{(1 - \frac{v_\mathrm{D}}{\varphi_\mathrm{J}})^{M_C}} \tag{27}$$

Thus, a comparison of (24) and (27) shows that the presented modeling is also in line with SPICE

models with:

$$M_C = \frac{1}{M+2} \tag{28}$$

However, in contrast to common SPICE models, the expansion of the SCR and the junction charge are described here as well, which is important for electro-optic modeling.

As the voltage v_D increases, the SCR width d_J decreases (see (13)). As soon as the SCR becomes very small and is on the order of the Debye length, the junction capacitance starts to deviate significantly from (24) [8]. Therefore, and in order to avoid discontinuities and poles at $v_\mathrm{D} = \varphi_\mathrm{J}$, a piecewise formulation with forward-bias coefficients FC_1, FC_2 and a Taylor approximation are applied:

$$C_j = \begin{cases} C_{\mathrm{j}0} \frac{1}{(1-\frac{v_\mathrm{D}}{\varphi_\mathrm{J}})^{M_C}}, & v_\mathrm{D} \leq FC_1\varphi_\mathrm{J} \\ C_{\mathrm{j}0} \frac{1-FC_1(M_C+1)+M_C\frac{v_\mathrm{D}}{\varphi_\mathrm{J}}}{(1-FC_1)^{M_C+1}}, & FC_1\varphi_\mathrm{J} < v_\mathrm{D}, \\ & v_\mathrm{D} \leq FC_2\varphi_\mathrm{J} \end{cases} \tag{29}$$

with

$$\begin{aligned} C_{\mathrm{j}0} =& A_\mathrm{J} \cdot \left(\frac{M_C \cdot e}{\varphi_\mathrm{J}}\right)^{M_C} \cdot \epsilon^{1-M_C} \\ & \cdot \left(C_\mathrm{D}^{\frac{M_C}{M_C-1}} + C_\mathrm{A}^{\frac{M_C}{M_C-1}}\right)^{M_C-1} \end{aligned} \tag{30}$$

and $FC_2 \geq FC_1$.

With $C_j = \frac{dq_\mathrm{J}}{dv_\mathrm{D}}$ and consideration of boundary conditions to fulfill continuity, the junction charge q_J results as:

$$q_\mathrm{J} = \begin{cases} q_{\mathrm{J}0} \cdot (1-\frac{v_\mathrm{D}}{\varphi_\mathrm{J}})^{1-M_C}, & \frac{v_\mathrm{D}}{\varphi_\mathrm{J}} \leq FC_1 \\ q_{\mathrm{J}0} \cdot \Big[(1-FC_1)^{1-M_C} & \\ -\frac{1-M_C}{(1-FC_1)^{M_C}}(\frac{v_\mathrm{D}}{\varphi_\mathrm{J}} - FC_1) & FC_1 < \frac{v_\mathrm{D}}{\varphi_\mathrm{J}}, \\ -\frac{M_C(1-M_C)\left(\frac{v_\mathrm{D}}{\varphi_\mathrm{J}}-FC_1\right)^2}{2(1-FC_1)^{M_C+1}}\Big], & \frac{v_\mathrm{D}}{\varphi_\mathrm{J}} \leq FC_2 \end{cases} \tag{31}$$

with $q_{\mathrm{J}0} = -\frac{C_{\mathrm{j}0}\cdot\varphi_\mathrm{J}}{1-M_C}$ according to (25) and (28).

Rearranging (21) and applying (28) yields:

$$\begin{aligned} d_\mathrm{J} =& \left(C_\mathrm{D}^{-\frac{M_C}{1-M_C}} + C_\mathrm{A}^{-\frac{M_C}{1-M_C}}\right) \\ & \cdot \left(\frac{1-M_C}{M_C A_\mathrm{J} e}\right)^{\frac{M_C}{1-M_C}} \cdot (-q_\mathrm{J})^{\frac{M_C}{1-M_C}} \end{aligned} \tag{32}$$

Considering (13) and (28) for $v_\mathrm{D} \leq FC_1 \cdot \varphi_\mathrm{J}$, (31) and (32) in the range $FC_1 < \frac{v_\mathrm{D}}{\varphi_\mathrm{J}} \leq FC_2$ and considering continuity, the SCR width d_J is described by:

$$d_\mathrm{J} = \begin{cases} d_{\mathrm{J}0} \cdot (1-\frac{v_\mathrm{D}}{\varphi_\mathrm{J}})^{M_C}, & \frac{v_\mathrm{D}}{\varphi_\mathrm{J}} \leq FC_1 \\ d_{\mathrm{J}0} \cdot \Big[(1-FC_1)^{1-M_C} & \\ -\frac{M_C(1-M_C)\left(\frac{v_\mathrm{D}}{\varphi_\mathrm{J}}-FC_1\right)^2}{2(1-FC_1)^{M_C+1}} & FC_1 < \frac{v_\mathrm{D}}{\varphi_\mathrm{J}}, \\ -\frac{(1-M_C)\left(\frac{v_\mathrm{D}}{\varphi_\mathrm{J}}-FC_1\right)}{(1-FC_1)^{M_C}}\Big]^{\frac{M_C}{1-M_C}}, & \frac{v_\mathrm{D}}{\varphi_\mathrm{J}} \leq FC_2 \end{cases} \tag{33}$$

with $d_{\mathrm{J}0} = A_\mathrm{J} \cdot \frac{\epsilon}{C_{\mathrm{j}0}}$ according to (26).

For voltages $v_\mathrm{D} > FC_2 \cdot \varphi_\mathrm{J}$, the PS becomes highly conductive and the SCR effectively vanishes. Although this operating region is not the focus of this work, the implemented model includes this operation region to avoid discontinuities, ensure numerically stable simulations, and allow further forward-bias modeling in future works. In those further works, a diffusion capacitance parallel to the junction capacitance would also be considered. A detailed description of the modeling for $v_\mathrm{D} > FC_2 \cdot \varphi_\mathrm{J}$ is given in Appendix A. Exemplary graphs of C_j, q_J, and d_J, including (29), (31), and (33), are shown in Fig. 4.

As Fig. 2 shows, the junction capacitor C_j is placed in series with a junction resistor r_J. This resistor models the nonlinear voltage-dependent ohmic resistance experienced by charge carriers when charging or discharging the junction. The experienced resistance in a semiconductor with length L, width w, height h, conductivity σ, electron mobility μ_e, free electron concentration N_e, hole mobility μ_h, and hole concentration N_h can be expressed as:

$$R = \int_0^L \frac{1}{\sigma A}\, dx = \int_0^L \frac{1}{wh(\mu_\mathrm{e}N_e + \mu_\mathrm{h}N_h)}\, dx \tag{34}$$

If we consider the p-type and n-type semiconductors separately without forming an SCR, constant resistances r_{p0} and r_{n0} are present in the p- and n-type semiconductor, respectively. Assuming a negligible concentration of free electrons in the p-doped semiconductor and a negligible concentration of holes in the n-doped semiconductor, the

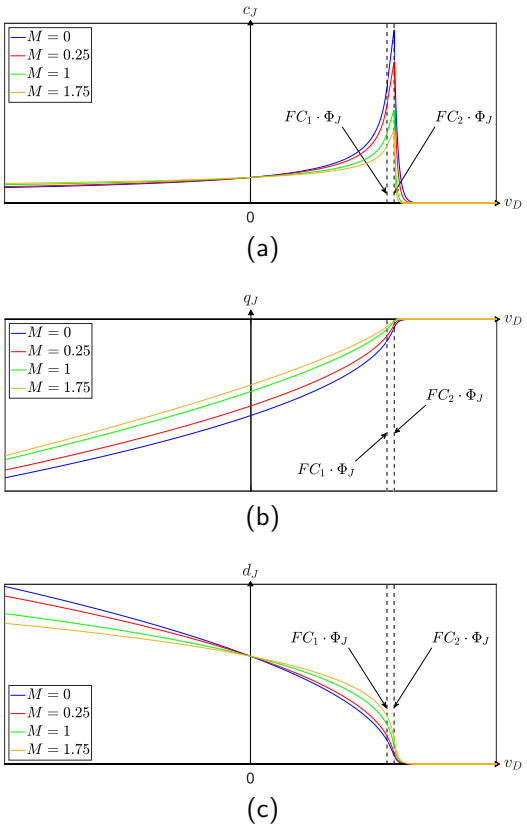


Fig. 4 (a) Junction capacitance C_j, (b) Junction charge q_J (c) SCR width over the applied voltage v_D for different gradient factors M (normalized to same zero-voltage junction capacitance C_j0)

total resistance can be expressed as:

$$\begin{aligned} r_\mathrm{J0} &= r_{p0} + r_{n0} \\ &\approx \frac{\frac{1}{\mu_\mathrm{h}} \int_{-\frac{w_\mathrm{PS}}{2}}^{0} \frac{1}{N_h}\, dx + \frac{1}{\mu_\mathrm{e}} \int_{0}^{\frac{w_\mathrm{PS}}{2}} \frac{1}{N_e}\, dx}{l_\mathrm{PS} h_\mathrm{PS}} \end{aligned} \tag{35}$$

Considering the SCR, the charge carriers pass a distance $d_p = \frac{w_\mathrm{PS}}{2} - x_\mathrm{p}$ in the p-doped semiconductor and a distance $d_n = \frac{w_\mathrm{PS}}{2} - x_\mathrm{n}$ in the n-doped semiconductor during charging and discharging processes. Therefore, the junction resistance r_J is given by:

$$\begin{aligned} r_\mathrm{J} &= r_\mathrm{p}(x_\mathrm{p}) + r_\mathrm{n}(x_\mathrm{n}) \\ &\approx \frac{\frac{1}{\mu_\mathrm{h}} \int_{-\frac{w_\mathrm{PS}}{2}}^{-x_\mathrm{p}} \frac{1}{N_h}\, dx + \frac{1}{\mu_\mathrm{e}} \int_{x_\mathrm{n}}^{\frac{w_\mathrm{PS}}{2}} \frac{1}{N_e}\, dx}{l_\mathrm{PS} \cdot h_\mathrm{PS}} \end{aligned} \tag{36}$$

With (35), the junction resistance r_J can be expressed with respect to r_J0:

$$\begin{aligned} r_\mathrm{J} &= r_\mathrm{J0} - \Delta r_\mathrm{J} \\ &\approx r_\mathrm{J0} - \frac{\frac{1}{\mu_\mathrm{h}} \int_{-x_\mathrm{p}}^{0} \frac{1}{N_h}\, dx + \frac{1}{\mu_\mathrm{e}} \int_{0}^{x_\mathrm{n}} \frac{1}{N_e}\, dx}{l_\mathrm{PS} h_\mathrm{PS}} \end{aligned} \tag{37}$$

Therefore, under consideration of $N_h = C_\mathrm{A} \cdot |x|^M$ and $N_e = C_\mathrm{D} \cdot |x|^M$, the junction resistance offset Δr_J results in:

$$\Delta r_\mathrm{J} = \frac{1}{l_\mathrm{PS} \cdot h_\mathrm{PS}} \cdot \frac{1}{1-M} \cdot \left(\frac{x_\mathrm{p}^{1-M}}{\mu_\mathrm{h} \cdot C_\mathrm{A}} + \frac{x_\mathrm{n}^{1-M}}{\mu_\mathrm{e} \cdot C_\mathrm{D}} \right) \tag{38}$$

Inserting (19) and (20) into (38) yields:

$$\Delta r_\mathrm{J} = \Delta r_\mathrm{J0} \cdot \left(1 - \frac{v_\mathrm{D}}{\varphi_\mathrm{J}}\right)^{\frac{1-M}{M+2}} \tag{39}$$

with

$$\begin{aligned} \Delta r_\mathrm{J0} = & \frac{d_\mathrm{J0}^{1-M}}{l_\mathrm{PS} \cdot h_\mathrm{PS}} \cdot \left[\frac{1}{\mu_\mathrm{h} C_\mathrm{A} \left(1 + \sqrt[M+1]{\frac{C_\mathrm{D}}{C_\mathrm{A}}}\right)^{1-M}} \right. \\ & \left. + \frac{1}{\mu_\mathrm{e} C_\mathrm{D} \left(1 + \sqrt[M+1]{\frac{C_\mathrm{A}}{C_\mathrm{D}}}\right)^{1-M}} \right] \cdot \frac{1}{1-M} \end{aligned} \tag{40}$$

In (36) the PS height h_PS is assumed to be constant, although every semiconductor manufacturing process is subject to process tolerances and non-ideal etching and polishing processes with anisotropy $\gamma < 1$, which lead to deviations from ideal rectangular rib structuring and height variations $h_\mathrm{PS}(x)$ in (34). Moreover, material boundaries with roughness and defect states also affect the junction resistance r_d. Therefore, the exponent in (39) is replaced by another ideality factor M_r, considering these deviations. Additionally, the case discrimination and Taylor approximation applied in (29) are employed in the junction resistance as well. Thus, the junction resistance r_J is

modeled as:

$$r_{\mathrm{J}} = \begin{cases} r_{\mathrm{J0}} - \Delta r_{\mathrm{J0}} \cdot (1 - \frac{v_{\mathrm{D}}}{\varphi_{\mathrm{J}}})^{1-M_r}, & \frac{v_{\mathrm{D}}}{\varphi_{\mathrm{J}}} \leq FC_1 \\ r_{\mathrm{J0}} - \Delta r_{\mathrm{J0}} \cdot \Big[(1 - FC_1)^{1-M_r} & \\ -\frac{1-M_r}{(1-FC_1)^{M_r}} \left(\frac{v_{\mathrm{D}}}{\varphi_{\mathrm{J}}} - FC_1 \right) \Big], & FC_1 < \frac{v_{\mathrm{D}}}{\varphi_{\mathrm{J}}} \end{cases} \tag{41}$$

It should be noted that the junction resistance r_{J} only covers the ohmic behavior of the semiconductor experienced by charge carriers within junction capacitance charging and discharging processes. The exponential diode behavior is still present and modeled by the ideal diode D in Fig. 2.

2.2 Small-signal phase shifter resistance and capacitance

The small-signal PS impedance is examined to enable interpretation and comparison between measurement results and modeling in later sections. Therefore, the electrical small-signal equivalent circuit presented in Fig. 5 is investigated. It is obtained by replacing the diode in Fig. 2 with its small-signal resistance r_{d}.

$$r_{\mathrm{d}} = \frac{\mathrm{d}v_{\mathrm{D}}}{\mathrm{d}i_{\mathrm{d}}} = \frac{n_{\mathrm{D}} \cdot V_{\mathrm{T}}}{I_{\mathrm{S}}} \cdot e^{-\frac{v_{\mathrm{D}}}{n_{\mathrm{D}} V_{\mathrm{T}}}} \tag{42}$$

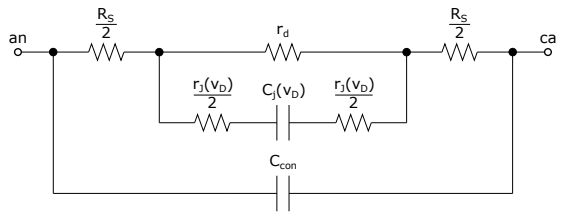


Fig. 5 Small-signal PS equivalent circuit

According to Fig. 5, the total PS small-signal-impedance can be derived as:

$$z_{\mathrm{ps}} = \frac{1}{\frac{1}{\tilde{z}_d + R_{\mathrm{S}}} + \frac{1}{jX_{C_{\mathrm{con}}}}} = \frac{\tilde{z}_d + R_{\mathrm{S}}}{1 + j\omega(\tilde{z}_d + R_{\mathrm{S}})C_{\mathrm{con}}} \tag{43}$$

with

$$\tilde{z}_{\mathrm{d}} = \frac{1}{\frac{1}{r_{\mathrm{d}}} + \frac{1}{r_{\mathrm{J}} + jX_{C_{\mathrm{j}}}}} = r_{\mathrm{d}} \cdot \frac{1 + j\omega r_{\mathrm{J}} C_{\mathrm{j}}}{1 + j\omega(r_{\mathrm{J}} + r_{\mathrm{d}})C_{\mathrm{j}}} \tag{44}$$

Approximating $r_{\mathrm{d}} \to \infty$ for voltages $V_{\mathrm{PS}} << 0$, $X_{C_{\mathrm{con}}} << \{X_{C_{\mathrm{j}}}, r_{\mathrm{d}}, r_{\mathrm{J}}\}$ for $0 < V_{\mathrm{PS}} < \varphi_{\mathrm{J}}$, and $r_{\mathrm{d}} \to 0$ for voltages $V_{\mathrm{PS}} >> \varphi_{\mathrm{J}}$ results in:

$$r_{\mathrm{ps}} = \Re(z_{\mathrm{ps}}) \approx \begin{cases} \frac{r_{\mathrm{J}} + R_{\mathrm{S}}}{(1 + \frac{C_{\mathrm{con}}}{C_{\mathrm{j}}})^2} & , V_{\mathrm{PS}} << 0 \\ R_{\mathrm{S}} + \frac{r_{\mathrm{d}} \cdot r_{\mathrm{J}}}{r_{\mathrm{d}} + r_{\mathrm{J}}} & , 0 < V_{\mathrm{PS}} < \varphi_{\mathrm{J}} \\ R_{\mathrm{S}} & , V_{\mathrm{PS}} >> \varphi_{\mathrm{J}} \end{cases} \tag{45}$$

$$\begin{aligned} C_{\mathrm{ps}} &= -\frac{1}{\omega \cdot \Im(z_{\mathrm{ps}})} \\ &\approx \begin{cases} C_{\mathrm{j}} + C_{\mathrm{con}} & , V_{\mathrm{PS}} << 0 \\ C_{\mathrm{j}} \cdot \left(1 + \frac{r_{\mathrm{J}}}{r_{\mathrm{d}}}\right)^2 & , 0 < V_{\mathrm{PS}} < \varphi_{\mathrm{J}} \\ \frac{1}{\omega^2 R_{\mathrm{S}}^2 C_{\mathrm{con}}} & , V_{\mathrm{PS}} >> \varphi_{\mathrm{J}} \end{cases} \end{aligned} \tag{46}$$

Further details on the applied approximations and derivation of (45) and (46) are given in Appendix B.

2.3 Optical modeling

An optical input signal $E(t, z)$ entering the PS

$$E(t, z) = E_0 \cdot e^{j\omega t} \cdot e^{-j\underline{k}z} \tag{47}$$

where $\underline{k}$ denotes the complex wavenumber

$$\underline{k} = \frac{2\pi}{\lambda_0}\underline{n} = \frac{2\pi}{\lambda_0} n_{\mathrm{eff}} - j\frac{2\pi}{\lambda_0}\kappa_{\mathrm{eff}} \,, \tag{48}$$

n_{eff} the refractive index, κ_{eff} the extinction coefficient, and λ_0 the optical wavelength in vacuum, leads to an optical output signal $E(t, l_{\mathrm{PS}})$, which can be described as [10]:

$$\begin{aligned} E(t, l_{\mathrm{PS}}) = & E_0 \cdot e^{j\omega t} \cdot e^{-j\phi_0} \cdot e^{-\frac{\alpha_0}{2} \cdot l_{\mathrm{PS}}} \\ & \cdot e^{-j\Delta\phi(q)} \cdot e^{-\frac{\Delta\alpha(q)}{2} \cdot l_{\mathrm{PS}}} \end{aligned} \tag{49}$$

in which the static and dynamic phase shifts and attenuation coefficients are defined as [10]:

$$\phi_0 = \frac{2\pi}{\lambda_0} \cdot n_{\mathrm{eff},0} \cdot l_{\mathrm{PS}} \tag{50}$$

$$\Delta\phi(v_{\mathrm{D}}) = \frac{2\pi}{\lambda_0} \cdot \Delta n_{\mathrm{eff}}(v_{\mathrm{D}}) \cdot l_{\mathrm{PS}} \tag{51}$$

$$\alpha_0 = \frac{2\pi}{\lambda_0} \cdot \kappa_{\mathrm{eff},0} \tag{52}$$

$$\Delta\alpha(v_{\mathrm{D}}) = \frac{2\pi}{\lambda_0} \cdot \Delta\kappa_{\mathrm{eff}}(v_{\mathrm{D}}) \tag{53}$$

In Fig. 2, the static phase shift ϕ_0 and static attenuation coefficient α_0 are modeled by conventional lossy waveguides. The static attenuation coefficient α_0 leads to the static insertion loss (IL):

$$IL^{(\mathrm{dB})} = -\,10\,\mathrm{dB}\log_{10}\left(\frac{P_{\mathrm{OUT}}}{P_{\mathrm{IN}}}\right) = \frac{10\,\mathrm{dB}\,l_{\mathrm{PS}}\alpha_0}{\log_{10}(e)} \tag{54}$$

The dynamic, voltage-dependent phase shift $\Delta\phi(v_{\mathrm{D}})$ and attenuation coefficient $\Delta\alpha(v_{\mathrm{D}})$ are represented by an inner E-to-O-converter block (see Fig. 2). According to the FCPD effect, changes in electron and hole concentrations cause changes in the refractive index n and the attenuation coefficient α [11]:

$$\Delta n = -\frac{e^2\cdot\lambda_0^2}{8\cdot\pi^2\cdot c_0^2\cdot\epsilon_0\cdot n}\cdot\left(\frac{\Delta N_e}{m_{\mathrm{e}}^*}+\frac{\Delta N_h}{m_{\mathrm{h}}^*}\right) \tag{55}$$

$$\Delta\alpha = \frac{e^3\cdot\lambda_0^2}{4\cdot\pi^2\cdot c_0^3\cdot\epsilon_0\cdot n}\cdot\left(\frac{\Delta N_e}{m_e^{*2}\cdot\mu_{\mathrm{e}}}+\frac{\Delta N_h}{m_h^{*2}\cdot\mu_{\mathrm{h}}}\right) \tag{56}$$

where c_0 denotes the speed of light in vacuum, ϵ_0 the vacuum permittivity, n the unperturbed refractive index, and N_e, N_h, m_{e}^*, m_{h}^*, μ_{e}, and μ_{h} the density, effective mass and mobility of free electrons and holes, respectively.
(55) and (56) cannot be directly applied to calculate the optical phase shift, because the charge carrier density and the electric field of the optical signal are not equally distributed. According to [12, 13], the spatial distribution can be taken into account by applying an overlap integral between the normalized optical intensity and the refractive index variation Δn to calculate the effective refractive index change Δn_{eff}. Considering that the optical intensity is proportional to the squared magnitude of the electric field, the refractive index change can be expressed as:

$$\Delta n_{\mathrm{eff}} \approx \frac{1}{A_{\mathrm{m}}}\iint_{A_{\mathrm{m}}}\Delta n(x,y)\cdot\left|\frac{E_0(x,y)}{\tilde{E}_0}\right|^2 dA \tag{57}$$

with $A_{\mathrm{m}} = d_{\mathrm{m}}h_{\mathrm{PS}}$ being the area in which the electric field is distributed, and normalization by means of $\tilde{E}_0 = E_0(x=0,y=0)$.
Inserting (55) yields:

$$\Delta n_{\mathrm{eff}} \approx \Delta n_{\mathrm{eff,h}} + \Delta n_{\mathrm{eff,e}} \tag{58}$$

with

$$\Delta n_{\mathrm{eff,h}} \approx -\frac{1}{A_{\mathrm{m}}}\iint_{A_{\mathrm{m}}}\frac{\Delta N_{\mathrm{h}}(x)}{N_{\mathrm{h,n1}}}\cdot\left|\frac{E_0(x,y)}{\tilde{E}_0}\right|^2 dA, \tag{59}$$

$$\Delta n_{\mathrm{eff,e}} \approx -\frac{1}{A_{\mathrm{m}}}\iint_{A_{\mathrm{m}}}\frac{\Delta N_{\mathrm{e}}(x)}{N_{\mathrm{e,n1}}}\cdot\left|\frac{E_0(x,y)}{\tilde{E}_0}\right|^2 dA, \tag{60}$$

with

$$N_{\mathrm{h,n1}} = \frac{8\cdot\pi^2\cdot c_0^2\cdot\epsilon_0\cdot n}{e^2\cdot\lambda_0^2}\cdot m_{\mathrm{h}}^*, \tag{61}$$

and

$$N_{\mathrm{e,n1}} = \frac{8\cdot\pi^2\cdot c_0^2\cdot\epsilon_0\cdot n}{e^2\cdot\lambda_0^2}\cdot m_{\mathrm{e}}^*. \tag{62}$$

The modeled PS is designed for single-mode input and output waveguide interfaces and the employed 250 nm EPIC BiCMOS technology only contains TE mode optimized grating couplers. Therefore, only the fundamental TE mode is considered here and no other modes are assumed to be guided. In a waveguide with sufficiently low propagation loss due to a negligibly small evanescent field outside of the waveguide, the optical mode can be approximated by a cosine field distribution inside the waveguide:

$$E_0(x,y) \approx \tilde{E}_0\cdot f(x)\cdot g(y) \tag{63}$$

with

$$f(x) = \begin{cases}\cos\left(\pi\cdot\frac{x}{d_{\mathrm{m}}}\right), & -\frac{d_{\mathrm{m}}}{2}\le x\le\frac{d_{\mathrm{m}}}{2}\\ 0, & |x|>\frac{d_{\mathrm{m}}}{2}\end{cases} \tag{64}$$

and

$$g(y) = \begin{cases}\cos\left(\frac{\pi}{2}\cdot\frac{y-y_0}{y_0}\right), & 0\le y\le y_0\\ \cos\left(\frac{\pi}{2}\cdot\frac{y-y_0}{h_{\mathrm{PS}}-y_0}\right), & y_0<y\le h_{\mathrm{PS}}\\ 0, & y<0 \text{ or } y>h_{\mathrm{PS}}\end{cases} \tag{65}$$

These assumptions were confirmed by EM simulations performed in Ansys Lumerical [14] that also show only one guided mode, which is presented in Fig. 6.

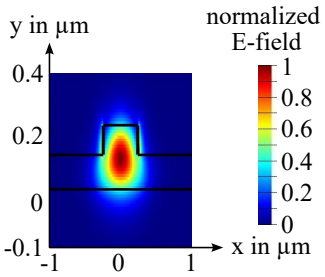


Fig. 6 Field distribution of the only guided optical mode found by the finite-difference Eigenmode solver in Ansys Lumerical

As further discussed in Section 3 and depicted in Fig. 7, the pn-junction is not placed in the center of the examined PSs, but near one of the rib edges. Thus, a generalization is introduced and the center of the pn-junction is considered to be located at position x_c.

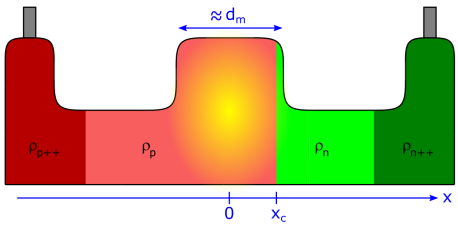


Fig. 7 PS cross section (the electric field distribution is indicated in yellow)

Since the charge distribution and, consequently, the refractive index change Δn are independent of y, substituting (63), (64), and (65) into (59) and (60) yields:

$$\Delta n_{\mathrm{eff,h}} = -\frac{1}{2d_\mathrm{m}} \int_{x_\mathrm{c}-x_\mathrm{p}}^{x_\mathrm{c}} \frac{\Delta N_\mathrm{h}(x)}{N_\mathrm{h,n1}} \cdot f^2(x)\, dx \quad (66)$$

and

$$\Delta n_{\mathrm{eff,e}} = -\frac{1}{2d_\mathrm{m}} \int_{x_\mathrm{c}}^{x_\mathrm{c}+x_\mathrm{n}} \frac{\Delta N_\mathrm{e}(x)}{N_\mathrm{e,n1}} \cdot f^2(x)\, dx \quad (67)$$

The charge carrier density does not change outside the SCR. Assuming that the charge carrier density within the SCR is negligibly small and that the charge carrier density prior to the formation of the SCR corresponds approximately to the doping concentration, the electron and hole concentration changes within the SCR are:

$$\Delta N_h = -C_\mathrm{A} \cdot |x - x_\mathrm{c}|^M, \quad \text{for } x_\mathrm{c} - x_\mathrm{p} \le x < x_\mathrm{c} \quad (68)$$

$$\Delta N_e = -C_\mathrm{D} \cdot (x - x_\mathrm{c})^M, \quad \text{for } x_\mathrm{c} < x \le x_\mathrm{c} + x_\mathrm{n} \quad (69)$$

Inserting (64), (68), and (69) into (66) and (67) leads to integrals that cannot be solved analytically for arbitrary M. Further details are given in Appendix C. Therefore, the refractive index change is instead approximated by the product of the average charge density change ΔN_av in the SCR and the overlap of the optical signal with the SCR:

$$\Delta n_{\mathrm{eff,h}} \approx -\frac{1}{A_\mathrm{m}} \frac{\Delta N_\mathrm{h,av}}{N_\mathrm{h,n1}} \cdot \iint\limits_{A_\mathrm{SCR,p}} \left| \frac{E_0(x,y)}{\tilde{E}_0} \right|^2 dA \quad (70)$$

$$\Delta n_{\mathrm{eff,e}} \approx -\frac{1}{A_\mathrm{m}} \frac{\Delta N_\mathrm{e,av}}{N_\mathrm{e,n1}} \cdot \iint\limits_{A_\mathrm{SCR,n}} \left| \frac{E_0(x,y)}{\tilde{E}_0} \right|^2 dA \quad (71)$$

with $A_\mathrm{SCR,p}$ and $A_\mathrm{SCR,n}$ being the areas of depleted p- and n-doped silicon, respectively.
The average charge density change is defined as the total charge change given in (18) divided by the volume:

$$\Delta N_\mathrm{h,av} = \frac{q_\mathrm{J}}{e x_\mathrm{p} l_\mathrm{PS} h_\mathrm{PS}} = -C_\mathrm{A} \cdot \frac{x_\mathrm{p}^M}{M+1} \quad (72)$$

$$\Delta N_\mathrm{e,av} = \frac{q_\mathrm{J}}{e x_\mathrm{n} l_\mathrm{PS} h_\mathrm{PS}} = -C_\mathrm{D} \cdot \frac{x_\mathrm{n}^M}{M+1} \quad (73)$$

Inserting into (70) and (71) results in:

$$\begin{aligned} \Delta n_{\mathrm{eff,h}} &\approx \frac{1}{A_\mathrm{m}} \frac{C_\mathrm{A} x_\mathrm{p}^M}{(M+1) N_\mathrm{h,n1}} \iint\limits_{A_\mathrm{SCR,p}} \left| \frac{E_0(x,y)}{\tilde{E}_0} \right|^2 dA \\ &= \frac{C_\mathrm{A} x_\mathrm{p}^M}{2d_\mathrm{m}(M+1) N_\mathrm{h,n1}} \cdot \int_{x_\mathrm{c}-x_\mathrm{p}}^{x_\mathrm{c}} f^2(x)\, dx \\ &= \frac{C_\mathrm{A} x_\mathrm{p}^M \left[\frac{x_\mathrm{p}}{d_\mathrm{m}} + \frac{\sin\left(2\pi \frac{x_\mathrm{c}}{d_\mathrm{m}}\right) - \sin\left(2\pi \frac{x_\mathrm{c}-x_\mathrm{p}}{d_\mathrm{m}}\right)}{2\pi} \right]}{4 N_\mathrm{h,n1}(M+1)} \end{aligned} \quad (74)$$

and

$$\Delta n_{\mathrm{eff,e}} \approx \frac{C_{\mathrm{D}} x_{\mathrm{n}}^{M} \left[\frac{x_{\mathrm{n}}}{d_{\mathrm{m}}} + \frac{\sin\left(2\pi \frac{x_{\mathrm{c}}+x_{\mathrm{n}}}{d_{\mathrm{m}}}\right) - \sin\left(2\pi \frac{x_{\mathrm{c}}}{d_{\mathrm{m}}}\right)}{2\pi} \right]}{4N_{\mathrm{e,n1}}(M+1)} \tag{75}$$

It should be noted that in case of $M = 0$, (74) and (75) are identical to (66) and (67), as shown in Appendix C, and therefore no error arises in the approximation. Furthermore, it should also be noted that in the presented derivations, it is assumed that the SCR does not exceed the approximated mode size ($|x_{\mathrm{c}} - x_{\mathrm{p}}| \leq \frac{d_{\mathrm{m}}}{2}$ and $|x_{\mathrm{c}} + x_{\mathrm{n}}| \leq \frac{d_{\mathrm{m}}}{2}$). Since this is not generally the case, other cases leading to modified integration boundaries are also taken into account. All further cases, which are considered in the derived PS model, are described in Appendix D.

Similar to the effective refractive index change Δn_{eff}, the attenuation constant change $\Delta\alpha$ is modeled as:

$$\Delta\alpha \approx \Delta\alpha_{\mathrm{h}} + \Delta\alpha_{\mathrm{e}} \tag{76}$$

with

$$\Delta\alpha_{\mathrm{h}} \approx -\frac{C_{\mathrm{A}} x_{\mathrm{p}}^{M} \left[\frac{x_{\mathrm{p}}}{d_{\mathrm{m}}} + \frac{\sin\left(2\pi \frac{x_{\mathrm{c}}}{d_{\mathrm{m}}}\right) - \sin\left(2\pi \frac{x_{\mathrm{c}}-x_{\mathrm{p}}}{d_{\mathrm{m}}}\right)}{2\pi} \right]}{4N_{\mathrm{h},\alpha 1}(M+1)} \tag{77}$$

and

$$\Delta\alpha_{\mathrm{e}} \approx -\frac{C_{\mathrm{D}} x_{\mathrm{n}}^{M} \left[\frac{x_{\mathrm{n}}}{d_{\mathrm{m}}} + \frac{\sin\left(2\pi \frac{x_{\mathrm{c}}+x_{\mathrm{n}}}{d_{\mathrm{m}}}\right) - \sin\left(2\pi \frac{x_{\mathrm{c}}}{d_{\mathrm{m}}}\right)}{2\pi} \right]}{4N_{\mathrm{e},\alpha 1}(M+1)} \tag{78}$$

for the case of $|x_{\mathrm{c}} - x_{\mathrm{p}}| \leq \frac{d_{\mathrm{m}}}{2}$ and $|x_{\mathrm{c}} + x_{\mathrm{n}}| \leq \frac{d_{\mathrm{m}}}{2}$,

$$N_{\mathrm{h},\alpha 1} = \frac{4 \cdot \pi^2 \cdot c_0^2 \cdot \epsilon_0 \cdot n}{e^2 \cdot \lambda_0^2} \cdot m_h^{*2} \cdot \mu_{\mathrm{h}} \tag{79}$$

and

$$N_{\mathrm{e},\alpha 1} = \frac{4 \cdot \pi^2 \cdot c_0^2 \cdot \epsilon_0 \cdot n}{e^2 \cdot \lambda_0^2} \cdot m_e^{*2} \cdot \mu_{\mathrm{e}} \,. \tag{80}$$

2.4 Model implementation

The presented model is implemented using the HDL Verilog-A to allow usage in common EDA IC design software [15]. It includes length scaling and all formulas derived in Subsections 2.1 to 2.3. The implemented Verilog-A code, which strictly follows the derived equations, is available in [16]. It allows simulation in conjunction with common SPICE models and parameter linking to layout cells, which enables efficient microchip design. Furthermore, it enables automated parameter optimization using EDA software to ensure optimal model parameter fitting.
To allow electro-optic co-simulations, optical signals were defined in a new Verilog-A discipline and all optical ports were assigned to this new discipline. All optical signals are defined as three-component vector signals, with the first component containing the real part of the electric field, the second component containing the imaginary part of the electric field and the last component containing the wavelength of the optical signal:

$$s_{\mathrm{opt}} = \begin{pmatrix} \Re(E) \\ \Im(E) \\ \lambda_{\mathrm{opt}} \end{pmatrix} \tag{81}$$

Due to the abstraction, the optical signals are reduced to their field strength, phase and wavelength. The high frequency of the optical wave is only taken into account in simulations by means of the wavelength in the third component of the vector, and only the envelope of the optical signal is calculated as a function of time within transient electro-optic simulations. As a result, the simulations can be carried out efficiently, even though the optical signals contain significantly higher frequencies than electrical signals.

3 Discussion of model parameters and doping profile improvement

The physical modeling approach used in the previous section implies that all model parameters can also be related to or directly derived from the geometry, material and dopant parameters used in fabrication. This is a major advantage over conventional phenomenological modeling, as bottlenecks of devices can also be identified and

optimizations of the fabrication process can be derived from the model. The novel approach of including the dopant gradient M in the PS modeling shows that the doping technique during the manufacturing process has a decisive influence on the device functionality. Spatially confined doping, with little dopant diffusion, for example by avoiding high process temperatures after doping, leads to a low gradient coefficient M, reduces the capacitance at high reverse voltages and reduces the junction resistance nonlinearity (see r_J becoming fully linear for $M = 0$ and $v_\mathrm{D} \leq FC_1\varphi_\mathrm{J}$ in (41)). It also leads to a higher slope in the SCR expansion $\frac{\mathrm{d}d_\mathrm{J}}{\mathrm{d}v_\mathrm{D}}$ (see Fig. 4c) and therefore to higher small-signal EO efficiency $\frac{\mathrm{d}\Delta\phi}{\mathrm{d}v_\mathrm{D}}$.
Only in the transition zone between p- and n-doped regions, where the SCR occurs in normal operation, is it assumed that the space charge density ρ is described by (3). Only when operating at high voltages v_D which would cause unnecessarily large phase shifts $\Delta\phi >> 2\pi$, ρ would approach the doping concentration levels N_A^- and N_D^+ in the p- and n-doped regions. Thus, (3) is not valid for unreasonably high voltages. In this case, ρ is limited to the implanted doping concentration levels N_A^- and N_D^+, and the factors C_A and C_D are proportional to the doping concentrations.

Taking into account (56) and considering that holes have a significantly higher effective mass in silicon than electrons, p-doped silicon leads to lower losses compared to n-doped silicon at comparable doping concentration [17]. Therefore, as depicted in Fig. 7 and described in Section 2.3, in the investigated PSs, the pn-junction is positioned close to the rib edge ($x_\mathrm{c} \approx \frac{d_\mathrm{m}}{2}$), so that the optical mode is mainly facing losses from holes, but not from electrons when no voltage is applied. Consequently, the IL is reduced.

As the measurement and parameter fitting process of the PS depicted in Fig. 7 revealed, the bandwidth was strongly limited by a large junction resistance r_J (presented in more detail in Section 5). To reduce the resistance and improve the PS bandwidth, a second PS geometry has been investigated, which is shown in Fig. 8, in which an additional doping implantation has been applied. However, as (26) shows, a homogeneous increase of doping concentrations over the entire PS would also result in an increase in junction capacitance, which would reduce the bandwidth instead.

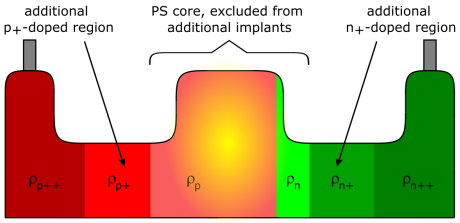


Fig. 8 Cross section of the PS with optimized doping profile

Moreover, it would also increase the number of mobile charge carriers and therefore, according to (56), it would also lead to increased static optical losses. Thus, the additional doping has been limited, excluding the PS core region in which the SCR occurs and the optical mode is confined (see Fig. 8). As it will be presented in Section 5, the PS region excluded from the additional doping was sized such that the PS capacitance was not measurably affected, but the resistance r_J was significantly reduced.

The measurement and parameter fitting process also revealed that although the voltage dependency of the SCR width described by (33) agrees well with the model, the pre-factor d_J0 does not correspond to $d_\mathrm{J0} = A_\mathrm{J} \cdot \frac{\epsilon}{C_\mathrm{j0}}$ when assuming the permittivity ϵ_i of intrinsic silicon. Doping affects the permittivity, but also crystal non-idealities and material interfaces may affect the permittivity. Therefore, an additional pre-factor N_dJ is used:

$$d_\mathrm{J0} = A_\mathrm{J} \cdot \frac{N_\mathrm{dJ} \cdot \epsilon_i}{C_\mathrm{j0}} \tag{82}$$

4 Measurement setup

In the following, three measurement setups, which were applied to both PSs types (see Fig. 7 and 8), are presented.

4.1 Y-parameter measurement

First, the PS was electrically characterized using the measurement setup depicted in Fig. 9. A vector network analyzer was connected to the PS via high-frequency cables and probes. Additionally, a voltage source was connected to the internal bias tees of the network analyzer to bias the PS. The bias voltage was swept, and Y-parameters were measured at each voltage step.

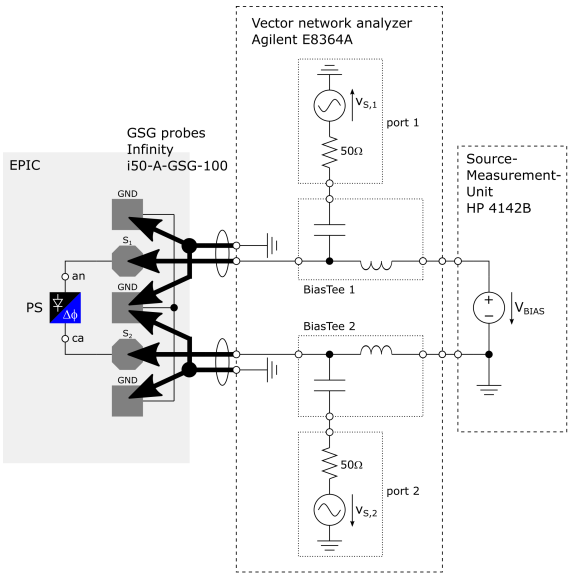


Fig. 9 Y-parameter measurement setup

4.2 Half-wave-voltage measurement

Another measurement setup used to extract the half-wave-voltage-length product $V_\pi L$ is presented in Fig. 10. As depicted, an external cavity laser with tunable output wavelength λ_{IN} generates an optical input signal. To ensure optimal coupling, the input signal polarization is adjusted using a polarization controller. It is then fed into an on-chip MZM including an optical delay line of length L_{dl} and group index $n_g(\lambda)$ in one arm and PSs in both arms. The MZM output signal is split into two signals, one of which is received by an optical power meter and the other by an optical spectrum analyzer. Only a small share of 10% is directed to the power meter, as it is used for automatic fiber alignment ensuring optimal coupling and measurement of PS losses.
The PS voltage v_{PS} and the input wavelength λ_{IN} were swept and the voltage-dependent optical spectrum $P_{\mathrm{opt,out}}(\lambda_{\mathrm{IN}}, v_{\mathrm{PS}})$ was measured at the spectrum analyzer.

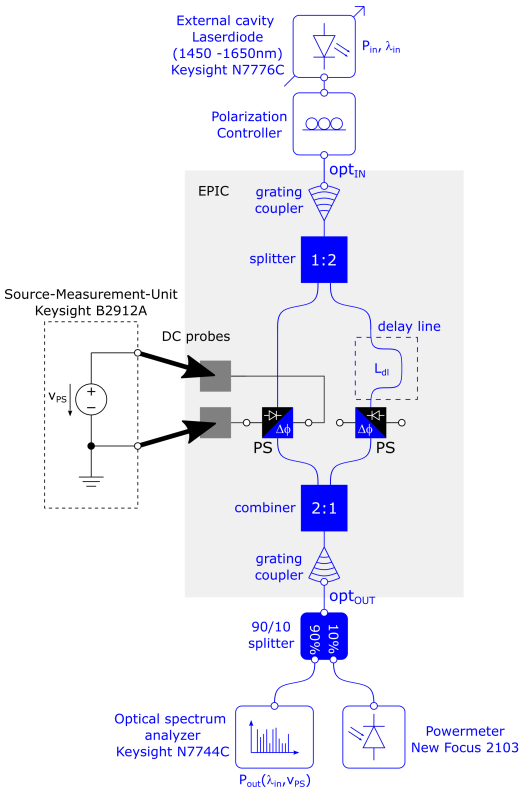


Fig. 10 Electro-optic measurement setup for $V_\pi L$ extraction

The delay line causes a wavelength-dependent phase shift

$$\Delta\phi_{\mathrm{dl}}(\lambda_{\mathrm{IN}}) = \frac{2\pi}{\lambda_{\mathrm{IN}}} n_{\mathrm{eff}}(\lambda_{\mathrm{IN}}) L_{\mathrm{DL}} \tag{83}$$

in one arm and the PS in the other arm causes a voltage-dependent phase shift

$$\Delta\phi_{\mathrm{PS}}(v_{\mathrm{PS}}) = \pi \cdot \frac{v_{\mathrm{PS}}}{V_\pi} \tag{84}$$

resulting in a phase difference $\Delta\phi$ between both arms:

$$\Delta\phi = \Delta\phi_{\mathrm{dl}} - \Delta\phi_{\mathrm{PS}} = \frac{2\pi}{\lambda_{\mathrm{IN}}} n_{\mathrm{eff}} L_{\mathrm{DL}} - \pi \cdot \frac{v_{\mathrm{PS}}}{V_\pi} \tag{85}$$

Assuming negligible differences in losses in both MZM arms, the transfer function of an MZM with insertion loss IL is

$$\frac{P_{\mathrm{opt,out}}}{P_{\mathrm{opt,in}}} = IL \cdot \left(\frac{1}{2} + \frac{1}{2}\cos\left(\Delta\phi\right)\right) \tag{86}$$

and the measured optical spectrum $P_{\mathrm{opt,out}}(\lambda_{\mathrm{IN}})$ can be expressed as:

$$\frac{P_{\mathrm{opt,out}}}{P_{\mathrm{opt,in}}} = IL\left[\frac{1}{2}+\frac{1}{2}\cos\left(\frac{2\pi}{\lambda_{\mathrm{IN}}}n_{\mathrm{eff}}L_{\mathrm{DL}}-\pi\frac{v_{\mathrm{PS}}}{V_\pi}\right)\right] \tag{87}$$

with minima at $\frac{2\pi}{\lambda_{\mathrm{IN}}}n_{\mathrm{eff}}L_{\mathrm{DL}}-\pi\cdot\frac{v_{\mathrm{PS}}}{V_\pi}=\pi\cdot(1+2m)$, $m\in\mathbb{Z}$.
Therefore, the positions of the minima in the optical spectrum change according to the applied PS voltage v_{PS} (see Fig. 11).

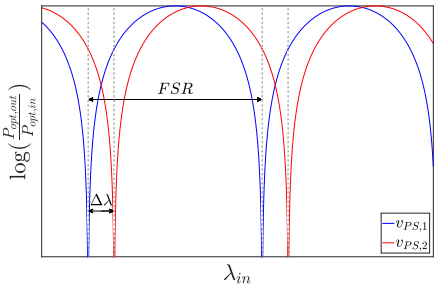


Fig. 11 Optical output spectrum for two different PS voltages v_{PS} when sweeping the input wavelength λ_{IN}

With the free spectral range (FSR) defined as the distance between two minima (see Fig. 11) and $\Delta\lambda$ being the shift when changing the PS voltage by Δv_{PS}, the voltage-induced phase shift $\Delta\phi_{\mathrm{PS}}$ can be derived. For an infinitesimally small wavelength shift of $\mathrm{d}\lambda$, the required phase shift $\mathrm{d}\phi_{\mathrm{PS}}$ is [18]:

$$\mathrm{d}\phi_{\mathrm{PS}} = \frac{2\pi}{FSR}\mathrm{d}\lambda \tag{88}$$

Thus, considering (84) and (88), the half-wave-voltage V_π can be determined by measuring the spectrum, extracting the FSR, and determining the inverse of the measured voltage-dependent shift $\frac{\mathrm{d}\lambda}{\mathrm{d}v_{\mathrm{PS}}}$:

$$V_\pi = \frac{1}{2}\cdot FSR\cdot\frac{\mathrm{d}v_{\mathrm{PS}}}{\mathrm{d}\lambda} \tag{89}$$

As only DC voltages are used in this measurement procedure and minima can be determined with high precision in the optical spectrum, this method allows accurate measurements of the half-wave-voltage V_π without inaccuracies due to frequency-dependent effects.

4.3 Insertion loss measurement

A third measurement setup was used to extract the PS loss (see Fig. 12). For this purpose, an optical signal was fed to a PS segment via grating couplers, while a reference structure was also fed to enable de-embedding of grating coupler losses. Thus, the output power $P_{\mathrm{OPT,OUT}}$ was measured and the PS insertion loss IL_{PS} is given by:

$$IL_{\mathrm{PS}}^{(\mathrm{dB})} = P_{\mathrm{OPT,OUT}}^{(\mathrm{dB})} - P_{\mathrm{OPT,IN}}^{(\mathrm{dB})} - 2\cdot IL_{\mathrm{GC}}^{(\mathrm{dB})} \tag{90}$$

where $P_{\mathrm{OPT,IN}}^{(\mathrm{dB})}$ denotes the optical input power and $IL_{\mathrm{GC}}^{(\mathrm{dB})}$ the grating coupler loss in decibels.

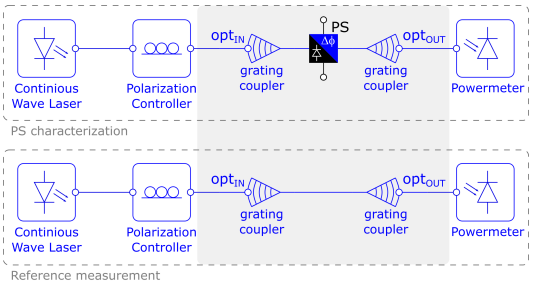


Fig. 12 Optical measurement setup for loss extraction

5 Parameter fitting process

5.1 Parameter fitting setup

The EDA software Keysight Advanced Design System [19] was used to perform Y-parameter, AC, and DC simulations and fit all model parameters. First, the Verilog-A PS model, following the mathematical descriptions derived in Section 2, was written and compiled. Afterwards, the testbench was set up. Y-parameter, AC, and DC simulation blocks, variables, optimizer, optimization goals, electrical and optical sources, as well as data access components to read measurement results, were placed and configured. The parameter fitting procedure, in which PS parameters are iteratively optimized until the PS characteristics match the measurement results, is depicted in Fig. 13. It was applied separately to both reverse-biased PS types using the corresponding measurement data.

First, an EM simulation was carried out using the manufacturer's layout and material stack files to extract the contact capacitance C_{con}. Second,

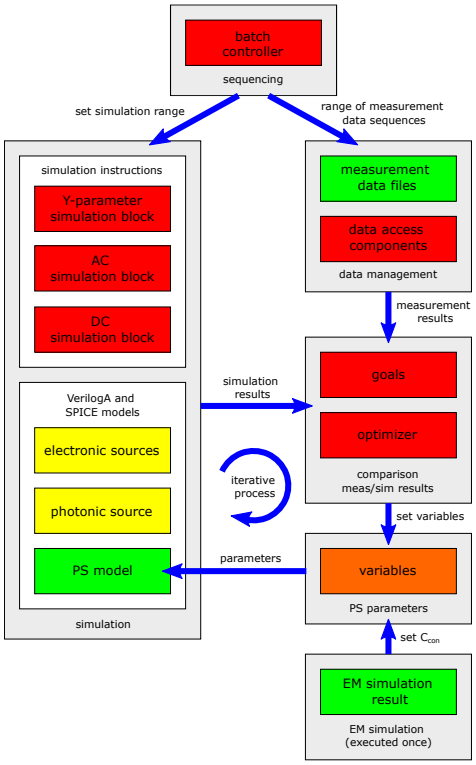


Fig. 13 Illustration of the simulation and parameter fitting process implemented in Keysight ADS (red: ADS components, green: files based on the findings of this work, orange: parameters, yellow: PDK components)

all remaining electrical parameters (I_S, n_D, R_S, C_j0, M_C, φ_J, r_J0, Δr_J0, M_r, FC_1, FC_2) were fitted to match the measured Y-parameters to the PS model, as they are independent of the measured optical characteristics. Afterwards, the remaining optical parameters (α_0, x_c, N_dJ, $N_\mathrm{h,n1}$, $N_\mathrm{e,n1}$, $N_\mathrm{h,\alpha1}$, and $N_\mathrm{e,\alpha1}$) were fitted to match the measured $V_\pi L$ and loss.

5.2 Parameter fitting results

To allow an easy interpretation and comparison of the Y-parameter measurement results with the derived formulas, the Y-parameters were converted into an equivalent resistance $R = -\Re(Y_{21}^{-1})$ and a capacitance $C = -(2\pi f)^{-1} \cdot \Im(Y_{21}^{-1})$ (see Fig. 14). It should be noted that the capacitance was only extracted for PS bias voltages V_PS below φ_J because strong noise contributions prevented reliable capacitance extraction from the measured Y-parameters beyond φ_J. From (45) and (46), it is apparent that the frequency dependence is negligibly small in the applied measurement range, which is in line with the measurement results shown in Fig. 14. Apart from small ripples, which are likely caused by the measurement equipment and limited calibration accuracy, the measured resistance does not show a strong frequency dependence. Furthermore, the capacitance is nearly constant up to frequencies of 30 GHz and shows a slight increase at higher frequencies where the approximations applied in (46) become less accurate.

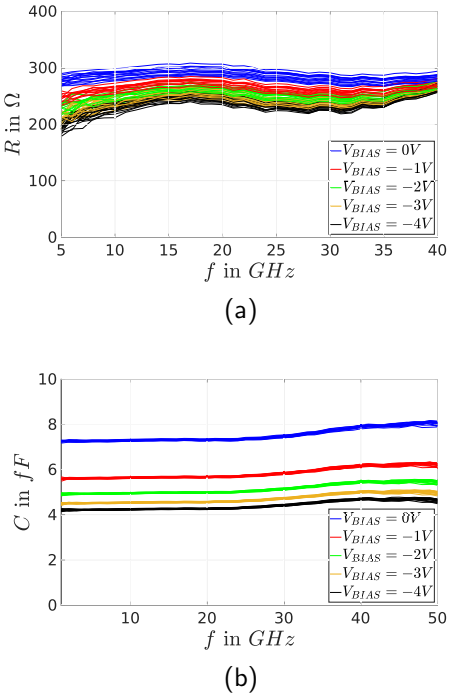


Fig. 14 Measured (a) resistance and (b) capacitance over frequency and voltage ($l_\mathrm{PS} = 20\,\mu$m, PS type 2)

Fig. 15a and 15b show the mean values of the measured resistance and capacitance (averaged over the range from 5 GHz to 30 GHz) and the simulation results after parameter fitting. Further details on the measurement sets are given in Appendix E.

Again, the measurement results are in good agreement with the applied equivalent circuit and the formulas derived in Section 2. At low voltages, the resistance is dominated by $r_\mathrm{J} + R_\mathrm{S}$ until the small-signal diode resistance r_d falls below r_J and, finally, the series resistance R_S dominates at high bias voltages. It can be seen that, as intended, the additional doping implants in PS type 2 only

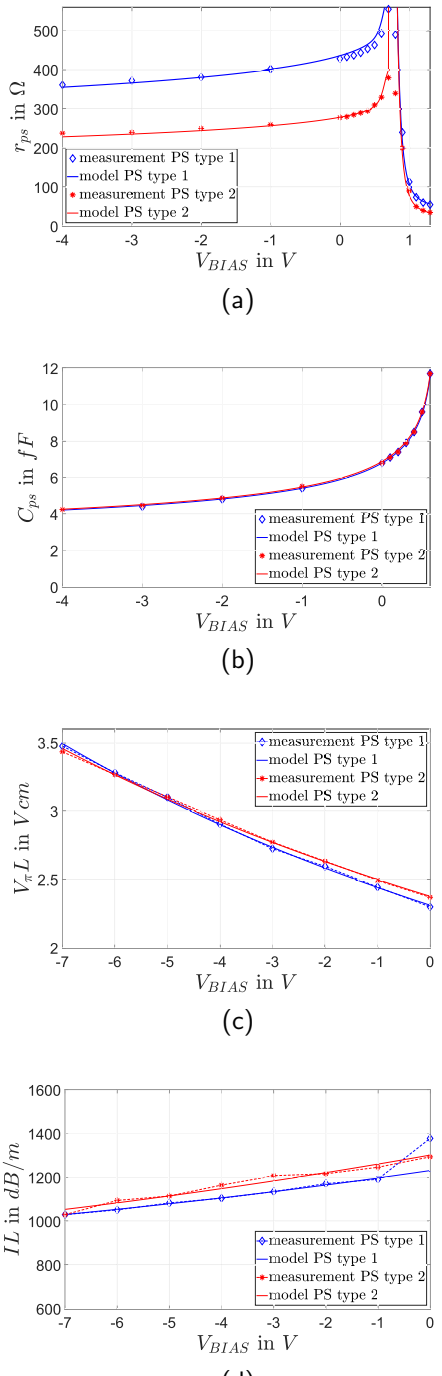


Fig. 15 Measured and simulated (a) resistance ($l_{\mathrm{PS}} = 20\,\mu\mathrm{m}$), (b) capacitance ($l_{\mathrm{PS}} = 20\,\mu\mathrm{m}$), (c) half-wave-voltage-length product $V_{\pi}L$, and (d) loss (averaged measurement results, further information given in Appendix E)

result in a measurable change in resistance, but not in any significant change in PS capacitance compared to PS type 1. Therefore, the PS bandwidth is significantly increased. Furthermore, the measurement and simulation results of the PS half-wave-voltage-length product $V_{\pi}L$ and loss are given in Fig. 15c and Fig. 15d. Apart from the insertion loss of the PS of type 1 measured at $0V$, which significantly deviates from the other insertion loss measurements and is explained by temporary displacement of the input fiber, leading to non-ideal coupling into the grating coupler in one of the measurement sets, all optical characteristics of the model are in very good agreement with the measured characteristics. In summary, Fig. 15 shows that the fitted PS model agrees well with the measurement results. An overview of all fitted model parameters is given in Table 1.

Table 1 Parameters of both investigated PSs (shown in Fig. 7 and Fig. 8) according to the new PS model (depicted in Fig. 2) at 1 mm length and 1550 nm input wavelength

Parameter	PS type 1	PS type 2
C_{con}	44.7 fF	44.7 fF
h_{PS}	220 nm	566 nm
d_{m}	555 nm	560 nm
I_{S}	89.4595 pA	24.957 15 nA
n_{D}	1.79288	1.68484
R_{S}	751.458 mΩ	374.858 mΩ
C_{j0}	296.98 fF	300.298 fF
M_C	0.304688	0.303726
φ_{J}	706.66 mV	705.298 mV
r_{J0}	33.4398 Ω	16.3601 Ω
Δr_{J0}	52.9742 mΩ	21.9368 mΩ
M_r	0.99766	0.99766
FC_1	0.954981	0.945616
FC_2	0.991884	1.008
γ	244	161
n_g	3.81	3.81
$IL^{(\mathrm{dB})}/l$, α_0	1322.53 $^{dB}/_{\mathrm{m}}$, 304.52 $^{1}/_{\mathrm{m}}$	1332.63 $^{dB}/_{\mathrm{m}}$, 306.85 $^{1}/_{\mathrm{m}}$
x_{c}	236 nm	230 nm
N_{dJ}	3.25	3.06
$N_{\mathrm{h,n1}}$	$6.25 \cdot 10^{-6}\,{}^{1}/_{m^2}$	$4.539 \cdot 10^{-6}\,{}^{1}/_{m^2}$
$N_{\mathrm{e,n1}}$	$4.167 \cdot 10^{-6}\,{}^{1}/_{m^2}$	$3.026 \cdot 10^{-6}\,{}^{1}/_{m^2}$
$N_{\mathrm{h},\alpha 1}$	$2.041 \cdot 10^{-11}\,{}^{1}/_{m^2}$	$1.673 \cdot 10^{-11}\,{}^{1}/_{m^2}$
$N_{\mathrm{e},\alpha 1}$	$1.14 \cdot 10^{-11}\,{}^{1}/_{m^2}$	$9.347 \cdot 10^{-12}\,{}^{1}/_{m^2}$

6 Electro-optic co-simulation of a high-speed transmitter

In the following, an electro-optic co-simulation of a reverse-biased silicon PS-based MZM with linear driver is discussed. The electro-optic transmitter is implemented in a 250 nm BiCMOS technology [5] and is presented in [20]. A segmented transmitter approach was chosen, dividing the 6.24 mm long PS into 16 PS segments with 390 μm length (see Fig. 16). An input amplifier drives 16 segment drivers, each of which drives a single PS segment. The input driver is connected to the segment drivers by means of velocity-matched transmission lines. The velocity matching between the electrical signal and the optical signal in the MZM ensures maximum electro-optic modulation efficiency and bandwidth [20–22].

As presented in [20], the transmitter allows higher data rates than all previously published transmitters in the same technology. During the design process, a conventional phenomenological RC PS model (depicted in Fig. 17) according to [23] was applied. All model parameters are presented in [20].

A comparison between measurement results and simulations shows that the conventional RC PS model does not sufficiently describe the high-frequency electro-optic response (see deviation between the green and the blue graphs in Fig. 18) and a more advanced PS model is required to allow precise simulations and improvements in high-speed transmitter design. Therefore, the new PS model, discussed in Sections 2 to 5, was developed and applied.

Fig. 18, Fig. 19, and Table 2 demonstrate the high accuracy of the developed model for both S-parameter and transient simulations. All relevant S21-parameter gradients, peaks and turning points are clearly captured by the new model (see red graph in Fig. 18), whereas they are not captured by the old model. Although the measurement shows an overshoot of approximately 2.7 dB, the simulation shows a smaller overshoot of approximately 2 dB, the 3 dB-bandwidth and the 6 dB-bandwidth of 24.2 GHz and 26.2 GHz are in good agreement with the measured bandwidths of 23.5 GHz and 26.7 GHz, respectively.
Furthermore, as can be seen in Fig. 19, the measured and simulated data rates of 60 Gb/s with non-return-to-zero (NRZ) and 80 Gb/s with 4-level pulse amplitude modulation (PAM4) match well.

Table 2 Resulting parameters from electro-optic transmitter S-parameter measurement and simulation

Parameter	Measurement result	RC PS model	New PS model
f_{3dB}	23.5 GHz	25.3 GHz	24.2 GHz
f_{6dB}	26.7 GHz	33.7 GHz	26.2 GHz
Overshooting	2.8 dB	0.65 dB	2 dB

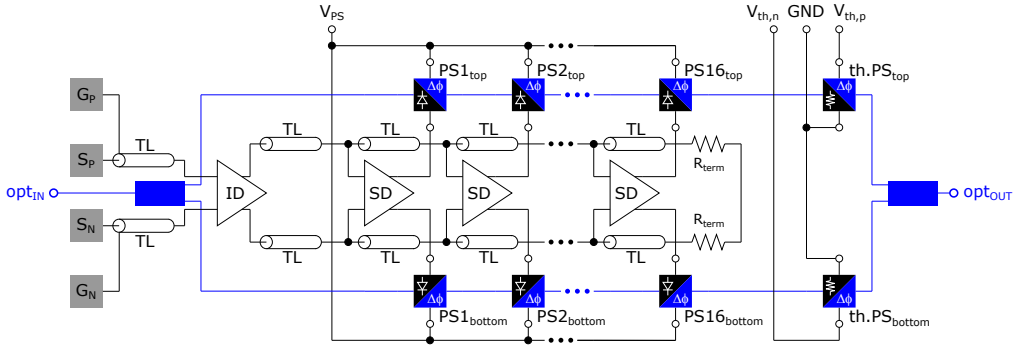


Fig. 16 TX structure with input pads, transmission lines (TL), input driver (ID), segment drivers (SD), TL termination resistors (R_{term}), reverse-biased PS and thermal PS

$$C_{\mathrm{D}}(v_{\mathrm{D}}) = (C_0 \cdot e^{\frac{v_{\mathrm{D}}}{V_2}} + C_1) \cdot L/m$$
$$\Delta n_{\mathrm{eff}}(v_{\mathrm{D}}) = \Delta n_{\mathrm{eff},0} \cdot (1 - e^{\frac{v_{\mathrm{D}}}{V_1}}) \cdot L/m$$

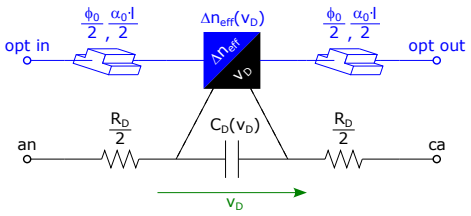


Fig. 17 Previously applied RC PS model (based on [23], applied in [20])

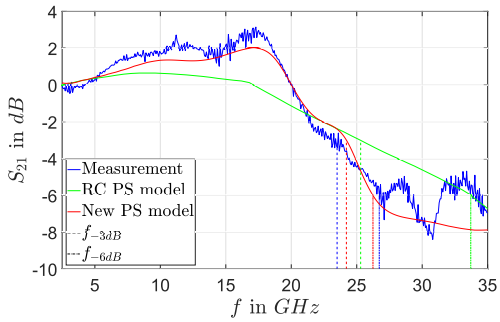


Fig. 18 Normalized S-parameter measurement and simulation results (green: model according to [20] and [23], red: new model developed in this work)

7 Conclusion

A model of a reverse-biased silicon PS has been derived and implemented. In contrast to common PS models, the presented model combines SPICE compatibility and physical modeling rather than phenomenological modeling. Therefore, it allows linking between parameters in the manufacturing process, in layout files and in the HDL code, and enables efficient electro-optic co-simulation in commonly used SPICE-based simulation environments.

Novel aspects of the model include the physical description of junction capacitance, junction resistance, charge, SCR expansion, and optical mode profile, taking into account non-homogeneous dopant concentrations. The approach uses parameters that are also employed in SPICE diode models to capture electrical behavior and are therefore well established, but to the best of the authors' knowledge have not previously been used for electro-optic modeling in any published FCPD-based PS model. Furthermore, the junction capacitance gradient exponent has not only been treated as an ideality factor as commonly done

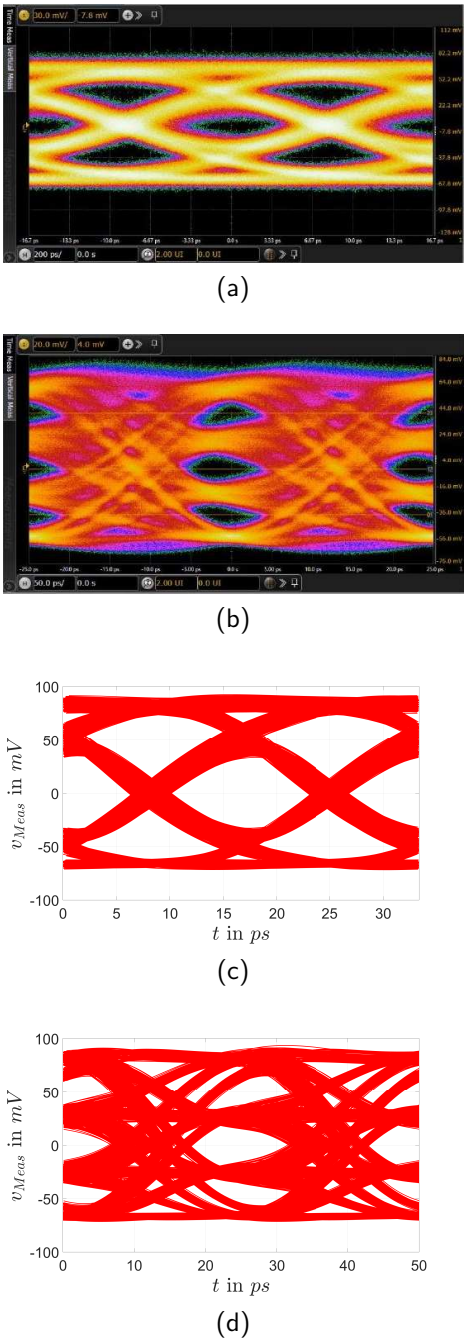


Fig. 19 Eye diagrams measured in a data transmission experiment (presented in [20]) and eye diagrams simulated with 100 ns simulation time, transient noise enabled, and PN31 pseudorandom binary sequence input signal
(a) measured with 60 Gb/s NRZ modulation
(b) measured with 80 Gb/s PAM4 modulation
(c) simulated with 60 Gb/s NRZ modulation
(d) simulated with 80 Gb/s PAM4 modulation

in SPICE models, but has also been investigated and linked to doping profiles. The derived model considers the spatially limited, voltage-dependent change in charge carrier density and reveals the significant influence of the doping concentration gradient in the pn-junction region. It allows identification of bottlenecks by linking PS behavior to the applied semiconductor technology and the parameters employed in the manufacturing process, as demonstrated by the example of a PS doping profile optimization. The high junction resistance has been identified as a bottleneck of the first PS and has been improved by another doping process step. According to the developed model, the PS core has been excluded from additional doping to ensure no increase in capacitance. The developed PS model has been analyzed analytically and measurement results match the outcome of the analysis. Moreover, a proof-of-concept has been given by application of the PS model to an electro-optic transmitter design. The transmitter, which shows data rates up to 80 Gbit/s in measurements, has been simulated and the simulations show excellent agreement with the measurement results.

Author contributions

Tobias Schwabe wrote the manuscript, developed and implemented the PS model, conducted analytical studies, analyzed the data, carried out the parameter fitting and simulations, and designed all electronic circuits and layouts of the investigated electro-optic high-speed transmitter. Daniel Steckler provided the PS measurements, while Christian Kress provided the transmitter measurements. Stephan Kruse contributed to technical discussions. Lars Zimmermann and Christoph J. Scheytt managed the project. All authors approved the final version of the manuscript.

Funding

This research was supported in part by the German Research Foundation (DFG) under Grant 403154102 and in part by the German Federal Ministry of Education and Research (BMBF) under Grant 13N14882.

Data availability

Simulation and measurement data underlying the results presented in this work may be obtained from the authors upon reasonable request. Details of the calculations and derivations are also available upon request. The implemented Verilog-A code is available at [16].

Declarations

Competing interests

The authors declare no competing interests.

Appendix A C_j, q_J, and d_J modeling in forward-bias operation

With effectively vanishing SCR, the junction capacitance as well as the offset junction charge must approach zero in order to be modeled physically correct:

$$C_\mathrm{j} \geq 0\ ,\ \lim_{v_\mathrm{D}\to\infty} C_\mathrm{j} \to 0 \tag{A1}$$

$$q_\mathrm{J} \leq 0\ ,\ \lim_{v_\mathrm{D}\to\infty} q_\mathrm{J} \to 0 \tag{A2}$$

Moreover, both variables must also fulfill mathematical continuity in order to ensure fault-free simulations. Consequently, considering (29), (31), and (33)

$$C_\mathrm{j}(FC_2\varphi_\mathrm{J}) = C_\mathrm{j0}\cdot\frac{1-FC_1(M_C+1)+M_C\cdot FC_2}{(1-FC_1)^{M_C+1}}, \tag{A3}$$

$$\begin{aligned} q_\mathrm{J}(FC_2\varphi_\mathrm{J}) = q_\mathrm{J0}\cdot\Bigg[&(1-FC_1)^{1-M_C} \\ &-\frac{1-M_C}{(1-FC_1)^{M_C}}(FC_2-FC_1) \\ &-\frac{1-M_C}{(1-FC_1)^{M_C+1}}\cdot\frac{M_C}{2}\cdot(FC_2-FC_1)^2\Bigg], \end{aligned} \tag{A4}$$

and

$$\begin{aligned} d_\mathrm{J}(FC_2\varphi_\mathrm{J}) = d_\mathrm{J0}\cdot\Bigg[&(1-FC_1)^{1-M_C} \\ &-\frac{1-M_C}{(1-FC_1)^{M_C+1}}\cdot\frac{M_C}{2}\cdot(FC_2-FC_1)^2 \\ &-\frac{1-M_C}{(1-FC_1)^{M_C}}\cdot(FC_2-FC_1)\Bigg]^{\frac{M_C}{1-M_C}} \end{aligned} \tag{A5}$$

have to be fulfilled.
Therefore, in forward-bias operation $v_\mathrm{D} > FC_2\cdot\varphi_\mathrm{J}$, the junction capacitance C_j, charge q_J, and SCR width d_J are defined as follows:

$$\begin{aligned} C_\mathrm{j} = [\ &C_\mathrm{j}(FC_2\varphi_\mathrm{J})\cdot(1-\gamma(v_\mathrm{D}-FC_2\varphi_\mathrm{J})) \\ &-q_\mathrm{J}(FC_2\varphi_\mathrm{J})\cdot(v_\mathrm{D}-FC_2\varphi_\mathrm{J})\cdot\gamma^2] \\ &\cdot e^{-\gamma(v_\mathrm{D}-FC_2\varphi_\mathrm{J})} \end{aligned} \tag{A6}$$

$$\begin{aligned} q_\mathrm{J} = [\ &q_\mathrm{J}(FC_2\varphi_\mathrm{J})\cdot(1+\gamma\cdot(v_\mathrm{D}-FC_2\varphi_\mathrm{J})) \\ &+C_\mathrm{j}(FC_2\varphi_\mathrm{J})\cdot(v_\mathrm{D}-FC_2\varphi_\mathrm{J})] \\ &\cdot e^{-\gamma(v_\mathrm{D}-FC_2\varphi_\mathrm{J})} \end{aligned} \tag{A7}$$

$$\begin{aligned} d_\mathrm{J} &= d_\mathrm{J}(FC_2\varphi_\mathrm{J})\cdot\left(\frac{q_\mathrm{J}}{q_\mathrm{J}(FC_2\varphi_\mathrm{J})}\right)^{\frac{M_C}{1-M_C}} \\ &= d_\mathrm{J}(FC_2\varphi_\mathrm{J})\cdot\Bigg[1+\gamma(v_\mathrm{D}-FC_2\varphi_\mathrm{J}) \\ &\quad+\frac{C_\mathrm{j}(FC_2\varphi_\mathrm{J})}{q_\mathrm{J}(FC_2\varphi_\mathrm{J})}\cdot(v_\mathrm{D}-FC_2\varphi_\mathrm{J})\Bigg]^{\frac{M_C}{1-M_C}} \\ &\quad\cdot e^{-\gamma\cdot(v_\mathrm{D}-FC_2\varphi_\mathrm{J})\cdot\frac{M_C}{1-M_C}} \end{aligned} \tag{A8}$$

with γ defining the velocity of the discharging process when the SCR is effectively vanishing.
To ensure no positive offset junction charge q_J and no negative junction capacitance C_j, the parameter γ has to satisfy

$$\gamma \geq -\frac{C_\mathrm{j}(FC_2\varphi_\mathrm{J})}{q_\mathrm{J}(FC_2\varphi_\mathrm{J})}\ . \tag{A9}$$

Further forward-bias PS modeling would also include the pn-junction diffusion capacitance C_d, which is rising with increased PS diode current i_d [6, 10]:

$$C_\mathrm{D} = \tau_\mathrm{TT}\cdot i_\mathrm{d} \tag{A10}$$

where τ_TT denotes the charge carrier transit time.

Appendix B Approximation of r_PS and C_PS

For negative bias voltages $V_\mathrm{PS} << 0$ the small-signal diode resistance r_d is very large and therefore it is neglected. Thus, with $r_\mathrm{d}\to\infty$, (43), and (44) it follows:

$$\begin{aligned} z_\mathrm{ps}^{(\mathrm{nv})} &\approx \frac{1}{\frac{1}{r_\mathrm{J}+\frac{1}{j\omega C_\mathrm{j}}+R_\mathrm{S}}+j\omega C_\mathrm{con}} \\ &= \frac{1+j\omega(r_\mathrm{J}+R_\mathrm{S})C_\mathrm{j}}{-\omega^2 C_\mathrm{j}C_\mathrm{con}(r_\mathrm{J}+R_\mathrm{S})+j\omega(C_\mathrm{j}+C_\mathrm{con})} \end{aligned} \tag{B11}$$

Conjugated complex expansion results in:

$$\begin{aligned} z_\mathrm{ps}^{(\mathrm{nv})} \approx &\frac{(r_\mathrm{J}+R_\mathrm{S})\cdot C_\mathrm{j}^2}{(C_\mathrm{j}+C_\mathrm{con})^2+\omega^2(r_\mathrm{J}+R_\mathrm{S})^2C_\mathrm{j}^2C_\mathrm{con}^2} \\ &-j\frac{(C_\mathrm{j}+C_\mathrm{con})+\omega^2(r_\mathrm{J}+R_\mathrm{S})^2C_\mathrm{j}^2C_\mathrm{con}}{\omega(C_\mathrm{j}+C_\mathrm{con})^2+\omega^3(r_\mathrm{J}+R_\mathrm{S})^2C_\mathrm{j}^2C_\mathrm{con}^2} \end{aligned} \tag{B12}$$

Therefrom, the effective PS resistance and capacitance follow as:

$$r_{\mathrm{ps}}^{(\mathrm{nv})} = \Re(z_{\mathrm{ps}}^{(\mathrm{nv})}) \approx \frac{r_{\mathrm{J}} + R_{\mathrm{S}}}{(1+\frac{C_{\mathrm{con}}}{C_{\mathrm{j}}})^2 + \omega^2 (r_{\mathrm{J}}+R_{\mathrm{S}})^2 C_{\mathrm{con}}^2} \tag{B13}$$

$$C_{\mathrm{ps}}^{(\mathrm{nv})} = -\frac{1}{\omega \cdot \Im(z_{\mathrm{ps}}^{(\mathrm{nv})})} \approx \frac{(C_{\mathrm{j}}+C_{\mathrm{con}})^2 + \omega^2 (r_{\mathrm{J}}+R_{\mathrm{S}})^2 C_{\mathrm{j}}^2 C_{\mathrm{con}}^2}{(C_{\mathrm{j}}+C_{\mathrm{con}}) + \omega^2 (r_{\mathrm{J}}+R_{\mathrm{S}})^2 C_{\mathrm{j}}^2 C_{\mathrm{con}}} \tag{B14}$$

With the parameters found within this work, $\omega^2 (r_{\mathrm{J}}+R_{\mathrm{S}})^2 C_{\mathrm{con}}^2 << 1$ and $\omega^2 (r_{\mathrm{J}}+R_{\mathrm{S}})^2 C_{\mathrm{j}} C_{\mathrm{con}} << 1$, apply for frequencies below 100 GHz, so that:

$$r_{\mathrm{ps}}^{(\mathrm{nv})} \approx \frac{r_{\mathrm{J}}+R_{\mathrm{S}}}{(1+\frac{C_{\mathrm{con}}}{C_{\mathrm{j}}})^2} \tag{B15}$$

$$C_{\mathrm{ps}}^{(\mathrm{nv})} \approx C_{\mathrm{j}} + C_{\mathrm{con}} \tag{B16}$$

For small positive bias voltages $0 < V_{\mathrm{PS}} < \varphi_{\mathrm{J}}$ the contact reactance $X_{C,con}$ is small compared to $X_{C_{\mathrm{j}}}$, r_{d} and r_{J}. Therefore, with (43), (44), and neglecting C_{con}, the PS impedance z_{ps} follows as:

$$z_{\mathrm{ps}}^{(\mathrm{sv})} \approx R_{\mathrm{S}} + r_{\mathrm{d}} \cdot \frac{1+j\omega r_{\mathrm{J}} C_{\mathrm{j}}}{1+j\omega(r_{\mathrm{d}}+r_{\mathrm{J}})C_{\mathrm{j}}} = R_{\mathrm{S}} + r_{\mathrm{d}} \cdot \frac{1-j\omega r_{\mathrm{d}} C_{\mathrm{j}} + \omega^2 r_{\mathrm{J}}(r_{\mathrm{d}}+r_{\mathrm{J}})C_{\mathrm{j}}^2}{1+\omega^2(r_{\mathrm{d}}+r_{\mathrm{J}})^2 C_{\mathrm{j}}^2} \tag{B17}$$

Therefrom, the effective PS resistance and capacitance follow as:

$$r_{\mathrm{ps}}^{(\mathrm{sv})} = \Re(z_{\mathrm{ps}}^{(\mathrm{sv})}) \approx R_{\mathrm{S}} + r_{\mathrm{d}} \cdot \frac{1+\omega^2 r_{\mathrm{J}}(r_{\mathrm{d}}+r_{\mathrm{J}})C_{\mathrm{j}}^2}{1+\omega^2(r_{\mathrm{d}}+r_{\mathrm{J}})^2 C_{\mathrm{j}}^2} = R_{\mathrm{S}} + \frac{r_{\mathrm{d}} \cdot r_{\mathrm{J}}}{r_{\mathrm{d}}+r_{\mathrm{J}}} \cdot \frac{1+\frac{1}{r_{\mathrm{J}}} \cdot \frac{1}{\omega^2(r_{\mathrm{d}}+r_{\mathrm{J}})C_{\mathrm{j}}^2}}{1+\frac{1}{r_{\mathrm{d}}+r_{\mathrm{J}}} \cdot \frac{1}{\omega^2(r_{\mathrm{d}}+r_{\mathrm{J}})C_{\mathrm{j}}^2}} \tag{B18}$$

$$C_{\mathrm{ps}}^{(\mathrm{sv})} = -\frac{1}{\omega \cdot \Im(z_{\mathrm{ps}}^{(\mathrm{sv})})} \approx \frac{1}{\omega} \cdot \frac{1+\omega^2(r_{\mathrm{d}}+r_{\mathrm{J}})^2 C_{\mathrm{j}}^2}{\omega r_{\mathrm{d}}^2 C_{\mathrm{j}}} = C_{\mathrm{j}} \cdot \left[\frac{1}{\omega^2 r_{\mathrm{d}}^2 C_{\mathrm{j}}^2} + \left(1+\frac{r_{\mathrm{J}}}{r_{\mathrm{d}}}\right)^2\right] \tag{B19}$$

$|\omega^2 C_{\mathrm{j}}^2| >> 1$ is assumed for $v_{\mathrm{D}} \approx \varphi_{\mathrm{J}}$ and it follows:

$$r_{\mathrm{ps}}^{(\mathrm{sv})} \approx R_{\mathrm{S}} + \frac{r_{\mathrm{d}} \cdot r_{\mathrm{J}}}{r_{\mathrm{d}}+r_{\mathrm{J}}} \tag{B20}$$

$$C_{\mathrm{ps}}^{(\mathrm{sv})} \approx C_{\mathrm{j}} \cdot \left(1+\frac{r_{\mathrm{J}}}{r_{\mathrm{d}}}\right)^2 \tag{B21}$$

For high bias voltages $V_{\mathrm{PS}} >> \varphi_{\mathrm{J}}$ the diode becomes highly conductive and r_{d} becomes negligibly small. Therefore, assuming $r_{\mathrm{d}} \to 0$, (43) and (44) result in:

$$z_{\mathrm{D}}^{(\mathrm{hv})} \to 0 \tag{B22}$$

$$z_{\mathrm{ps}}^{(\mathrm{hv})} \approx \frac{1}{\frac{1}{R_{\mathrm{S}}} + \frac{1}{jX_{C_{\mathrm{con}}}}} = \frac{R_{\mathrm{S}}}{1+j\omega R_{\mathrm{S}} C_{\mathrm{con}}} = \frac{R_{\mathrm{S}} - j\omega R_{\mathrm{S}}^2 C_{\mathrm{con}}}{1+\omega^2 R_{\mathrm{S}}^2 C_{\mathrm{con}}^2} \tag{B23}$$

Since $\omega^2 R_{\mathrm{S}}^2 C_{\mathrm{con}}^2 << 1$ is valid for frequencies below 100 GHz, the PS resistance simplifies to:

$$r_{\mathrm{ps}}^{(\mathrm{hv})} = \Re(z_{\mathrm{ps}}^{(\mathrm{hv})}) \approx \frac{R_{\mathrm{S}}}{1+\omega^2 R_{\mathrm{S}}^2 C_{\mathrm{con}}^2} \approx R_{\mathrm{S}} \tag{B24}$$

and the capacitance is

$$C_{\mathrm{ps}}^{(\mathrm{hv})} = -\frac{1}{\omega \cdot \Im(z_{\mathrm{ps}}^{(\mathrm{hv})})} \approx C_{\mathrm{con}} + \frac{1}{\omega^2 R_{\mathrm{S}}^2 C_{\mathrm{con}}} \approx \frac{1}{\omega^2 R_{\mathrm{S}}^2 C_{\mathrm{con}}} \tag{B25}$$

Appendix C Discussion of the integral for refractive index calculation

Inserting (64), (68), and (69) into (66) and (67) leads to

$$\Delta n_{\mathrm{eff,h}} = \frac{C_{\mathrm{A}} \int_{x_{\mathrm{c}}-x_{\mathrm{p}}}^{x_{\mathrm{c}}} (x_{\mathrm{c}}-x)^M \cos^2\left(\pi \cdot \frac{x}{d_{\mathrm{m}}}\right) dx}{2 d_{\mathrm{m}} N_{\mathrm{h,n1}}} \tag{C26}$$

and

$$\Delta n_{\mathrm{eff,e}} = \frac{C_{\mathrm{D}} \int_{x_{\mathrm{c}}}^{x_{\mathrm{c}}+x_{\mathrm{n}}} (x-x_{\mathrm{c}})^M \cos^2\left(\pi \cdot \frac{x}{d_{\mathrm{m}}}\right) dx}{2 d_{\mathrm{m}} N_{\mathrm{e,n1}}} \tag{C27}$$

The integrals cannot be solved generally for all M. In case of $M = 0$ they follow in:

$$\Delta n_{\mathrm{eff,h}} = \frac{C_{\mathrm{A}} \int_{x_{\mathrm{c}}-x_{\mathrm{p}}}^{x_{\mathrm{c}}} \cos^2\left(\pi \cdot \frac{x}{d_{\mathrm{m}}}\right) dx}{2 d_{\mathrm{m}} N_{\mathrm{h,n1}}}$$
$$= \frac{C_{\mathrm{A}}}{4 N_{\mathrm{h,n1}}} \left(\frac{\sin\left(2\pi \frac{x_{\mathrm{c}}}{d_{\mathrm{m}}}\right) - \sin\left(2\pi \frac{x_{\mathrm{c}}-x_{\mathrm{p}}}{d_{\mathrm{m}}}\right)}{2\pi} + \frac{x_{\mathrm{p}}}{d_{\mathrm{m}}} \right) \tag{C28}$$

$$\Delta n_{\mathrm{eff,e}} = \frac{C_{\mathrm{D}} \int_{x_{\mathrm{c}}}^{x_{\mathrm{c}}+x_{\mathrm{n}}} \cos^2\left(\pi \cdot \frac{x}{d_{\mathrm{m}}}\right) dx}{2 d_{\mathrm{m}} N_{\mathrm{e,n1}}}$$
$$= \frac{C_{\mathrm{D}}}{4 N_{\mathrm{e,n1}}} \left(\frac{\sin\left(2\pi \frac{x_{\mathrm{c}}+x_{\mathrm{n}}}{d_{\mathrm{m}}}\right) - \sin\left(2\pi \frac{x_{\mathrm{c}}}{d_{\mathrm{m}}}\right)}{2\pi} + \frac{x_{\mathrm{n}}}{d_{\mathrm{m}}} \right) \tag{C29}$$

Appendix D Case distinction for the refractive index calculation

Considering $A_{\mathrm{m}} = d_{\mathrm{m}} \cdot h_{\mathrm{PS}}$ and considering $x_{\mathrm{min,p}}$ and $x_{\mathrm{max,p}}$ being the boundaries of the depleted p-doped silicon overlapping with the optical signal in x-direction, (70) follows in:

$$\Delta n_{\mathrm{eff,h}} \approx - \frac{\Delta N_{\mathrm{h,av}} \int_0^{h_{\mathrm{PS}}} \int_{x_{\mathrm{min,p}}}^{x_{\mathrm{max,p}}} \left| \frac{E_0(x,y)}{\bar{E}_0} \right|^2 dx\, dy}{d_{\mathrm{m}} h_{\mathrm{PS}} N_{\mathrm{h,n1}}} \tag{D30}$$

Taking into account the electric field distribution according to (63), (64), and (65) follows in:

$$\Delta n_{\mathrm{eff,h}} \approx -\frac{1}{2 d_{\mathrm{m}}} \frac{\Delta N_{\mathrm{h,av}}}{N_{\mathrm{h,n1}}} \cdot \int_{x_{\mathrm{min,p}}}^{x_{\mathrm{max,p}}} f^2(x)\, dx \tag{D31}$$

$\Delta N_{\mathrm{h,av}}$ is the average of the charge density change in the region in which the optical signal and the charge density change overlap:

$$\Delta N_{\mathrm{h,av}} = \frac{\int_0^{h_{\mathrm{PS}}} \int_{x_{\mathrm{min,p}}}^{x_{\mathrm{max,p}}} \Delta N_{\mathrm{h}}(x)\, dx\, dy}{h_{\mathrm{PS}}(x_{\mathrm{max,p}} - x_{\mathrm{min,p}})} \tag{D32}$$

Solving the integral with respect to y and inserting (68) leads to:

$$\Delta N_{\mathrm{h,av}} = -\frac{C_{\mathrm{A}} \cdot \int_{x_{\mathrm{min,p}}}^{x_{\mathrm{max,p}}} |x - x_{\mathrm{c}}|^M\, dx}{x_{\mathrm{max,p}} - x_{\mathrm{min,p}}} \tag{D33}$$

Thus, (D33) can be inserted into (D31) to derive

$$\Delta n_{\mathrm{eff,h}} \approx \frac{C_{\mathrm{A}} \int_{x_{\mathrm{min,p}}}^{x_{\mathrm{max,p}}} |x - x_{\mathrm{c}}|^M dx \int_{x_{\mathrm{min,p}}}^{x_{\mathrm{max,p}}} f^2(x) dx}{2 d_{\mathrm{m}} N_{\mathrm{h,n1}} \cdot (x_{\mathrm{max,p}} - x_{\mathrm{min,p}})}. \tag{D34}$$

Similarly, $\Delta n_{\mathrm{eff,e}}$ follows as:

$$\Delta n_{\mathrm{eff,e}} \approx \frac{C_{\mathrm{D}} \int_{x_{\mathrm{min,n}}}^{x_{\mathrm{max,n}}} |x - x_{\mathrm{c}}|^M dx \int_{x_{\mathrm{min,n}}}^{x_{\mathrm{max,n}}} f^2(x) dx}{2 d_{\mathrm{m}} N_{\mathrm{e,n1}} \cdot (x_{\mathrm{max,n}} - x_{\mathrm{min,n}})} \tag{D35}$$

where $x_{\mathrm{min,n}}$ and $x_{\mathrm{max,n}}$ denote the boundaries of the depleted n-doped silicon overlapping with the optical signal in x-direction.
Inserting the boundaries for the individual cases leads to the results presented in table D1 and D2.

Table D1 Effective refractive index change caused by the hole concentration change

case	$\Delta n_{\mathrm{eff,h}}$
$x_{\mathrm{c}} < -\frac{d_{\mathrm{m}}}{2}$	0
$x_{\mathrm{c}} - x_{\mathrm{p}} \leq -\frac{d_{\mathrm{m}}}{2}$, $\lvert x_{\mathrm{c}} \rvert \leq \frac{d_{\mathrm{m}}}{2}$	$\frac{C_{\mathrm{A}} \cdot (x_{\mathrm{c}} + \frac{d_{\mathrm{m}}}{2})^M}{4 N_{\mathrm{h,n1}} \cdot (M+1)} \cdot \left[\frac{1}{2\pi} \sin\left(2\pi \frac{x_{\mathrm{c}}}{d_{\mathrm{m}}}\right) + \frac{x_{\mathrm{c}}}{d_{\mathrm{m}}} + \frac{1}{2} \right]$
$\lvert x_{\mathrm{c}} - x_{\mathrm{p}} \rvert < \frac{d_{\mathrm{m}}}{2}$, $\lvert x_{\mathrm{c}} \rvert \leq \frac{d_{\mathrm{m}}}{2}$	$\frac{C_{\mathrm{A}} \cdot x_{\mathrm{p}}^M}{4 N_{\mathrm{h,n1}} \cdot (M+1)} \cdot \left[\frac{1}{2\pi} \sin\left(2\pi \frac{x_{\mathrm{c}}}{d_{\mathrm{m}}}\right) - \frac{1}{2\pi} \sin\left(2\pi \frac{x_{\mathrm{c}}-x_{\mathrm{p}}}{d_{\mathrm{m}}}\right) + \frac{x_{\mathrm{p}}}{d_{\mathrm{m}}} \right]$
$\lvert x_{\mathrm{c}} - x_{\mathrm{p}} \rvert < \frac{d_{\mathrm{m}}}{2}$, $\frac{d_{\mathrm{m}}}{2} < x_{\mathrm{c}}$	$\frac{C_{\mathrm{A}} \cdot \left[x_{\mathrm{p}}^{M+1} - \left(x_{\mathrm{c}} - \frac{d_{\mathrm{m}}}{2}\right)^{M+1} \right]}{4 N_{\mathrm{h,n1}} \cdot (\frac{d_{\mathrm{m}}}{2} - x_{\mathrm{c}} + x_{\mathrm{p}}) \cdot (M+1)} \cdot \left[\frac{1}{2\pi} \sin\left(2\pi \frac{x_{\mathrm{p}}-x_{\mathrm{c}}}{d_{\mathrm{m}}}\right) + \frac{1}{2} - \frac{x_{\mathrm{c}}-x_{\mathrm{p}}}{d_{\mathrm{m}}} \right]$
$\frac{d_{\mathrm{m}}}{2} \leq x_{\mathrm{c}} - x_{\mathrm{p}}$	0
$x_{\mathrm{c}} - x_{\mathrm{p}} \leq -\frac{d_{\mathrm{m}}}{2}$, $\frac{d_{\mathrm{m}}}{2} \leq x_{\mathrm{c}}$	$\frac{C_{\mathrm{A}} \cdot \left[\left(x_{\mathrm{c}} + \frac{d_{\mathrm{m}}}{2}\right)^{M+1} - \left(x_{\mathrm{c}} - \frac{d_{\mathrm{m}}}{2}\right)^{M+1} \right]}{4 d_{\mathrm{m}} N_{\mathrm{h,n1}} \cdot (M+1)}$

Table D2 Effective refractive index change caused by the free electron concentration change

case	$\Delta n_{\mathrm{eff,e}}$
$\frac{d_\mathrm{m}}{2} < x_\mathrm{c}$	0
$\frac{d_\mathrm{m}}{2} < x_\mathrm{c} + x_\mathrm{n}$, $\lvert x_\mathrm{c}\rvert \leq \frac{d_\mathrm{m}}{2}$	$\frac{C_\mathrm{D}\cdot\left(\frac{d_\mathrm{m}}{2}-x_\mathrm{c}\right)^M}{4N_\mathrm{e,n1}\cdot(M+1)} \cdot\left[-\frac{1}{2\pi}\sin\left(2\pi\frac{x_\mathrm{c}}{d_\mathrm{m}}\right)+\frac{1}{2}-\frac{x_\mathrm{c}}{d_\mathrm{m}}\right]$
$\lvert x_\mathrm{c}+x_\mathrm{n}\rvert \leq \frac{d_\mathrm{m}}{2}$, $-\frac{d_\mathrm{m}}{2} \leq x_\mathrm{c}$	$\frac{C_\mathrm{D}\cdot x_\mathrm{n}^M}{4N_\mathrm{e,n1}\cdot(M+1)} \cdot\left[-\frac{1}{2\pi}\sin\left(2\pi\frac{x_\mathrm{c}}{d_\mathrm{m}}\right) +\frac{1}{2\pi}\sin\left(2\pi\frac{x_\mathrm{c}+x_\mathrm{n}}{d_\mathrm{m}}\right)+\frac{x_\mathrm{n}}{d_\mathrm{m}}\right]$
$\lvert x_\mathrm{c}+x_\mathrm{n}\rvert \leq \frac{d_\mathrm{m}}{2}$, $x_\mathrm{c} \leq -\frac{d_\mathrm{m}}{2}$	$\frac{C_\mathrm{D}\cdot\left[x_\mathrm{n}^{M+1}-(-\frac{d_\mathrm{m}}{2}-x_\mathrm{c})^{M+1}\right]}{4N_\mathrm{e,n1}\cdot(x_\mathrm{n}+\frac{d_\mathrm{m}}{2}+x_\mathrm{c})\cdot(M+1)} \cdot\left[\frac{1}{2\pi}\sin\left(2\pi\frac{x_\mathrm{c}+x_\mathrm{n}}{d_\mathrm{m}}\right)+\frac{x_\mathrm{c}+x_\mathrm{n}}{d_\mathrm{m}}+\frac{1}{2}\right]$
$x_\mathrm{c}+x_\mathrm{n} \leq -\frac{d_\mathrm{m}}{2}$	0
$\frac{d_\mathrm{m}}{2} \leq x_\mathrm{c}+x_\mathrm{n}$, $x_\mathrm{c} \leq -\frac{d_\mathrm{m}}{2}$	$\frac{C_\mathrm{D}\cdot\left[(\frac{d_\mathrm{m}}{2}-x_\mathrm{c})^{M+1}-(-\frac{d_\mathrm{m}}{2}-x_\mathrm{c})^{M+1}\right]}{4N_\mathrm{e,n1}\cdot d_\mathrm{m}\cdot(M+1)}$

Appendix E Measurement sets

The measurement sets listed in table E3 were conducted to extract the PS parameters.

Table E3 Measurement sets

PS type	Measured quantity	Measure-ments	Device length (in mm)	Bias voltage range (in V)
1	Y	3	0.02	−3 to 1.3
1	$V\pi L$	3	2 & 4	0 to 7
1	IL	3	20	0 to 7
2	Y	10	0.02	−4 to 0
2	Y	3	0.02	−3 to 1.3
2	$V\pi L$	3	2 & 4	0 to 7
2	IL	4	20	0 to 7

References

[1] Png, C.E., Sun, M.J., Lim, S.T., Ogawa, K.: Analysis of depletion silicon phase shifter based on computer simulation. In: Reed, G.T., Knights, A.P. (eds.) Silicon Photonics XI, vol. 9752, p. 975204. SPIE, Bellingham, WA (2016). https://doi.org/10.1117/12.2210895 . International Society for Optics and Photonics

[2] Sugesh, R.G.J., Sivasubramanian, A.: Modelling and Analysis of a Corrugated PN Junction Phase Shifter in Silicon MZM. Silicon **14**, 2669–2677 (2022) https://doi.org/10.1007/s12633-021-00990-z . Springer

[3] Begović, A., Kim, Y.H., Jiang, L., Anderson, S., Huang, Z.R.: Low VπLπ and Driving Voltage Interleaved Silicon Phase Shifter for Modulation Applications. IEEE Photonics Journal **14**(3), 1–6 (2022) https://doi.org/10.1109/JPHOT.2022.3170046

[4] Nagel, L.W.: SPICE2: A Computer Program to Simulate Semiconductor Circuits. PhD thesis, EECS Department, University of California, Berkeley (May 1975). http://www2.eecs.berkeley.edu/Pubs/TechRpts/1975/9602.html

[5] Knoll, D., Lischke, S., Awny, A., Kroh, M., Krune, E., Mai, C., Peczek, A., Petousi, D., Simon, S., Voigt, K., Winzer, G., Barth, R., Zimmermann, L.: High-performance BiCMOS Si photonics platform. In: 2015 IEEE Bipolar/BiCMOS Circuits and Technology Meeting - BCTM, pp. 88–96 (2015). https://doi.org/10.1109/BCTM.2015.7340583

[6] Reisch, M.: Halbleiter-Bauelemente, 2nd edn., pp. 47–85. Springer, Berlin, Heidelberg, New York, Germany, USA (2007). Chap. 2

[7] Fukuda, M.: Optical Semiconductor Devices, 1st edn., pp. 56–73. Wiley and Sons, Inc., New York, Chichester, Weinheim, Brisbane, Singapore, Toronto (1999). Chap. 2

[8] Müller, R.: Grundlagen der Halbleiter-Elektronik, 7th edn., pp. 129–142. Springer, Berlin, Heidelberg (1995). Chap. 7

[9] Simon M. Sze, M.-K.L.: Semiconductor Devices Physics and Technology, 3rd edn., pp. 84–96. John Wiley and Sons, Inc., 605 Third Avenue, New York, NY 10158-0012 (2012). Chap. 3

[10] Schwabe, T., Kress, C., Kruse, S., Weizel, M., Rhee, H., Scheytt, J.C.: Forward-Biased Silicon Phase Shifter Modeling for Electronic-Photonic Co-Simulation and Validation in a 250 nm EPIC BiCMOS Technology. Journal of Lightwave Technology **43**(1), 255–270 (2025) https://doi.org/10.1109/JLT.2024.3450949

[11] Soref, R., Bennett, B.: Electrooptical effects

in silicon. IEEE Journal of Quantum Electronics **23**(1), 123–129 (1987) https://doi.org/10.1109/JQE.1987.1073206

[12] Rasigade, G., Marris-Morini, D., Ziebell, M., Cassan, E., Vivien, L.: Analytical model for depletion-based silicon modulator simulation. Opt. Express **19**(5), 3919–3924 (2011) https://doi.org/10.1364/OE.19.003919

[13] Schermer, R.T., Bucholtz, F., Villarruel, C.A., Gil, J.G., Andreadis, T.D., Williams, K.J.: Investigation of electrooptic modulator disruption by microwave-induced transients. Opt. Express **17**(25), 22586–22602 (2009) https://doi.org/10.1364/OE.17.022586

[14] Ansys, I.: Ansys Lumerical. https://www.ansys.com/de-de/products/optics/mode. Accessed: 2025-12-08 (2025)

[15] Designer's Guide Consulting, I.: Verilog-AMS Language Reference Manual. https://designers-guide.org/verilog-ams/VlogAMS-2.4.0.pdf. Accessed: 2024-08-23 (2024)

[16] Schwabe, T., Kress, C., Scheytt, J.C.: SPICE-Compatible Electronic–Photonic Model Library. Zenodo (2026). https://doi.org/10.5281/zenodo.18935579

[17] Becker, J., Fretwurst, E., Klanner, R.: Measurements of charge carrier mobilities and drift velocity saturation in bulk silicon of ⟨111⟩ and ⟨100⟩ crystal orientation at high electric fields. Solid-State Electronics **56**(1), 104–110 (2011) https://doi.org/10.1016/j.sse.2010.10.009

[18] Kim, G., Park, J.W., Kim, I.G., Kim, S., Kim, S., Lee, J.M., Park, G.S., Joo, J., Jang, K.-S., Oh, J.H., Kim, S.A., Kim, J.H., Lee, J.Y., Park, J.M., Kim, D.-W., Jeong, D.-K., Hwang, M.-S., Kim, J.-K., Park, K.-S., Chi, H.-K., Kim, H.-C., Kim, D.-W., Cho, M.H.: Low-voltage high-performance silicon photonic devices and photonic integrated circuits operating up to 30 Gb/s. Opt. Express **19**(27), 26936–26947 (2011) https://doi.org/10.1364/OE.19.026936

[19] Technologies, K.: Keysight Advanced Design System (ADS). https://www.keysight.com/de/de/products/software/pathwave-design-software/pathwave-advanced-design-system.html. Accessed: 2024-08-23 (2024)

[20] Kress, C., Schwabe, T., Rhee, H., Christoph Scheytt, J.: Compact, High-Speed Mach-Zehnder Modulator With On-Chip Linear Drivers in Photonic BiCMOS Technology. IEEE Access **12**, 64561–64570 (2024) https://doi.org/10.1109/ACCESS.2024.3396877

[21] Chung, H., Chang, W.S.C., Adler, E.L.: Modeling and optimization of traveling-wave LiNbO3 interferometric modulators. IEEE Journal of Quantum Electronics **27**, 608–617 (1991) https://doi.org/10.1109/3.81370

[22] Samani, A., Chagnon, M., Patel, D., Veerasubramanian, V., Ghosh, S., Osman, M., Zhong, Q., Plant, D.V.: A Low-Voltage 35-GHz Silicon Photonic Modulator-Enabled 112-Gb/s Transmission System. IEEE Photonics Journal **7**(3), 1–13 (2015) https://doi.org/10.1109/JPHOT.2015.2426875

[23] Petousi, D.: Analysis of Integrated Silicon Depletion-Type Mach-Zehnder Modulators for Advanced Modulation Formats. Phd thesis, Berlin Institute of Technology, Berlin, CE (September 2017). Chap. 4, 5. https://tu-berlin.hosted.exlibrisgroup.com/permalink/f/1ljtibe/TUB_ALMA_DS21575612460002884